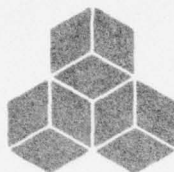


(12) LEVEL II



SYSTEMS, SCIENCE AND SOFTWARE

AD A067643

DDC FILE COPY

SSS-R-78-3736

SOURCE STUDIES, RESULTS FROM THE DISCRIMINATION
EXPERIMENT AND SUMMARY OF CURRENT RESEARCH

J. M. SAVINO
N. RIMER
H. J. SWANGER
T. C. BACHE

QUARTERLY TECHNICAL REPORT
FOR PERIOD APRIL 1 - JUNE 30, 1978

SPONSORED BY
ADVANCED RESEARCH PROJECTS AGENCY
ARPA ORDER No. 2551

DDC
RECEIVED
APR 19 1979
B

This research was supported by the Advanced Research Projects Agency of the Department of Defense and was monitored by AFTAC/VSC, Patrick Air Force Base, Florida, 32925, under Contract No. F08606-76-C-0041.

The views and conclusions contained in this document are those of the authors and should not be interpreted as necessarily representing the official policies, either expressed or implied, of the Advanced Research Projects Agency, the Air Force Technical Applications Center, or the U. S. Government.

APPROVED FOR PUBLIC RELEASE, DISTRIBUTION UNLIMITED
AUGUST 1978

P. O. BOX 1620, LA JOLLA, CALIFORNIA 92038, TELEPHONE (714) 453-0060

79 04 17 046

AFTAC Project Authorization No. VELA/T/7712/B/ETR

ARPA Order 2551, Program Code 8F10

Effective Date of Contract: October 1, 1976

Contract Expiration Date: September 30, 1978

Amount of Contract: \$435,087

Contract No. F08606-76-C-0041

Principal Investigator and Phone No.

Dr. Thomas C. Bache, (714) 453-0060, Ext. 337

Project Scientist and Phone No.

Captain Michael J. Shore, (202) 325-7581

Unclassified

SECURITY CLASSIFICATION OF THIS PAGE (When Data Entered)

REPORT DOCUMENTATION PAGE		READ INSTRUCTIONS BEFORE COMPLETING FORM
1. REPORT NUMBER	2. GOVT ACCESSION NO.	3. RECIPIENT'S CATALOG NUMBER
4. TITLE (and Subtitle) SOURCE STUDIES, RESULTS FROM THE DISCRIMINATION EXPERIMENT AND SUMMARY OF CURRENT RESEARCH,		5. TYPE OF REPORT & PERIOD COVERED Quarterly Report 4-1-78 to 6-30-78
7. AUTHOR(s) J. M. Savino, H. J. Swanger N. Rimer, T. E. Bache Thomas C. Bache		6. PERFORMING ORG. REPORT NUMBER SSS-R-78-3736
9. PERFORMING ORGANIZATION NAME AND ADDRESS Systems, Science and Software P. O. Box 1620 La Jolla, California 92038		10. PROGRAM ELEMENT, PROJECT, TASK AREA & WORK UNIT NUMBERS F08606-76-C-0041 ARPA Order-2551
11. CONTROLLING OFFICE NAME AND ADDRESS VELA Seismological Center 312 Montgomery Street Alexandria, Virginia 22314		12. REPORT DATE August 1978
14. MONITORING AGENCY NAME & ADDRESS (if different from Controlling Office) 76 p		13. NUMBER OF PAGES 68
		15. SECURITY CLASS. (of this report) Unclassified
		15a. DECLASSIFICATION DOWNGRADING SCHEDULE
16. DISTRIBUTION STATEMENT (of this Report) Approved for Public Release, Distribution Unlimited.		
17. DISTRIBUTION STATEMENT (of the abstract entered in Block 20, if different from Report) Quarterly technical rept. 1 Apr-30 Jun 78,		
18. SUPPLEMENTARY NOTES		
19. KEY WORDS (Continue on reverse side if necessary and identify by block number) Nuclear Explosion Seismology Seismic Source Theory Seismic Discrimination		
20. ABSTRACT (Continue on reverse side if necessary and identify by block number) Brief summaries of work currently underway or completed during the period from 1 April to 31 June 1978 are given in four topic areas: Source Studies, Data Analysis, Surface Wave Studies and Body Wave Studies. The remainder of the report is devoted to presentation of results not previously reported from three research projects. (continued)		

Unclassified

SECURITY CLASSIFICATION OF THIS PAGE(When Data Entered)

20. ABSTRACT (continued)

(research update describes a)
The first is entitled "Discrimination Experiment." Digital short and long period body and surface wave data for Eurasian events recorded at a global network of stations are being provided for event discrimination. Efforts to date have focused on the application of the VFM (Variable Frequency Magnitude) discriminant to the short period P waves at eight stations. Twenty-eight events *were* analyzed and tentative identification ~~has been~~ made.

The second project is entitled; "Surface Wave Solution for the Elastic Equivalent of a Complex Axisymmetric Source." In our last quarterly report we presented the mathematical development of a method for linking finite difference numerical source calculations with analytical technicals for propagating body waves in layered elastic media. In this report the theory is extended to include the propagation of Rayleigh waves.

The third project is entitled; "Source Calculations." Our one-dimensional constitutive models for the numerical simulation of the explosion source were reviewed to ensure their compatibility with our two-dimensional finite difference programs. Three important improvements to the models were made: (1) the implementation of new equations of state for the cavity gases; (2) an improved treatment of overburden pressure and (3) an improved effective stress model. The new models and their effect on source calculations for PILEDRIVER, SALMON and Rainier Mesa tuff are described.

ACCESSION for	
NTIS	White Section <input checked="" type="checkbox"/>
DDC	Buff Section <input type="checkbox"/>
UNANNOUNCED	<input type="checkbox"/>
JUSTIFICATION	
BY	
DISTRIBUTION/AVAILABILITY CODES	
Dist. AVAIL. and/or SPECIAL	
A	

Unclassified

SECURITY CLASSIFICATION OF THIS PAGE(When Data Entered)

TABLE OF CONTENTS

<u>Section</u>		<u>Page</u>
I.	INTRODUCTION AND SUMMARY.	1
1.1	BACKGROUND	1
1.2	SUMMARY OF RESEARCH DURING THIS QUARTER.	1
1.3	SUMMARY OF SECTION II: "DISCRIMINATION EXPERIMENT".	5
1.4	SUMMARY OF SECTION III: "SURFACE WAVE SOLUTION FOR THE ELASTIC EQUIVALENT OF A COMPLEX AXISYMMETRIC SOURCE	6
1.5	SUMMARY OF SECTION IV: "SOURCE CALCULATIONS".	6
II.	DISCRIMINATION EXPERIMENT	8
2.1	INTRODUCTION	8
2.2	DESCRIPTION OF DATA.	8
2.3	DISCRIMINATION RESULTS	12
2.4	SUMMARY.	33
III.	SURFACE WAVE SOLUTION FOR THE ELASTIC EQUIVALENT OF A COMPLEX AXISYMMETRIC SOURCE.	36
3.1	INTRODUCTION	36
3.2	THEORETICAL DEVELOPMENT.	37
3.3	IMPLEMENTATION	48
IV.	SOURCE CALCULATIONS	50
	REFERENCES.	67

LIST OF ILLUSTRATIONS

<u>Figure</u>		<u>Page</u>
2.1	Map of Eurasia showing locations of events and several of the stations included in the discrimination experiment.	9
2.2a	Short-period seismogram for the P wave recorded at Bluff, Alaska (BFAK) from event 47	13
2.2b	Group arrival time (t_g) as a function of filter center frequency (f_c) for event 47 recorded at Bluff, Alaska (BFAK)	15
2.2c	Sum of the envelope amplitudes plotted as a function of time after origin time for event 47 recorded at Bluff, Alaska (BFAK). . .	16
2.3a	Short-period seismogram of P wave recorded at Bluff, Alaska (BFAK) from event 53.	18
2.3b	Group arrival time (t_g) as a function of filter center frequency (f_c) for event 53 recorded at Bluff, Alaska (BFAK)	19
2.3c	Sum of the envelope amplitudes plotted as a function of time after origin time for event 53 recorded at Bluff, Alaska (BFAK). . .	20
2.4a	Variable frequency magnitude, $\bar{m}_b(f)$, estimates, not corrected for noise, at $f_c = 0.5$ Hz and 3.0 Hz for events recorded at Bluff, Alaska (BFAK).	21
2.4b	Variable frequency magnitude, $\bar{m}_b(f)$, estimates, not corrected for noise, at 0.55 Hz and 3.0 Hz for events recorded at Bluff, Alaska (BFAK).	22
2.4c	Variable frequency magnitude, $\bar{m}_b(f)$, estimates, not corrected for noise, at 0.5 Hz and 3.5 Hz for events recorded at Bluff, Alaska (BFAK).	23
2.5a	Noise corrected $\bar{m}_b(f)$ estimates for events recorded at BFAK	25
2.5b	Noise corrected $\bar{m}_b(f)$ estimates for events recorded at BFAK	26

LIST OF ILLUSTRATIONS (continued)

<u>Figure</u>		<u>Page</u>
2.6	Variable frequency magnitude, $\bar{m}_b(f)$, estimates not corrected for noise, at $f_c = 0.45$ Hz and 2.25 Hz based on short-period P waves recorded at ANMO and LAO	27
2.7	Variable frequency magnitude, $\bar{m}_b(f)$, estimates, not corrected for noise, for events recorded at the Iranian array (ILPA)	28
2.8	Variable frequency magnitude, $\bar{m}_b(f)$, estimates, not corrected for noise, for events recorded at the SRO station in Kabul, Afghanistan (KAAO)	29
2.9	Variable frequency magnitude, $\bar{m}_b(f)$, estimates, not corrected for noise, for events recorded at the Korean array (KSRS)	30
2.10	Variable frequency magnitude, $\bar{m}_b(f)$, estimates, not corrected for noise, for events recorded at the SRO station in Charters Towers, Australia (CTAO)	31
2.11	Variable frequency magnitude, $\bar{m}_b(f)$, estimates, not corrected for noise, for events recorded at the SRO station in Chaing Mai, Thailand (CHTO)	32
3.1	Source-receiver geometry for point forces present on the source cylinder	40
4.1	Particle velocity versus time at a range of 668 feet for PILEDRIVER (61 kt) calculation 411.	54
4.2	Particle velocity versus time at a range of 1543 feet for PILEDRIVER (61 kt) calculation 411.	55
4.3	Equivalent source functions for PILEDRIVER calculations	57
4.4	Equivalent source functions for SALMON calculations	59
4.5	Equivalent source functions for Area 12 tuff	62

LIST OF TABLES

<u>Table</u>		<u>Page</u>
2.1	Event Location Information	10
2.2	Status of Data Base: June 30, 1978.	11
2.3	Preliminary Event Identification	34
4.1	Material Properties Used for Source Function Calculations.	51

I. INTRODUCTION AND SUMMARY

1.1 BACKGROUND

The objective of the Systems, Science and Software (S³) research program is to examine the parameters that affect the seismic signals from underground explosions and earthquakes. Attention is primarily directed to those features of the seismic waveforms that discriminate between the two classes of events and that reliably indicate the explosion yield. Current research includes empirical studies of the available data, time signal analysis, and the development and application of theoretical and numerical methods for modeling earthquakes and explosions. Emphasis is on the last of these. In particular, we are applying techniques for theoretically simulating the far-field signatures of simple and complex seismic sources.

This report summarizes the work done during the seventh three-month period of the current contract.

1.2 SUMMARY OF RESEARCH DURING THIS QUARTER

Our work during this quarter has included research in a number of areas. Research projects currently underway or completed during the quarter are briefly summarized below.

Source Studies

A. Earthquake Modeling on the ILLIAC IV Computer

A three-dimensional finite difference program for modeling earthquake faulting has been made operational on the ILLIAC IV computer. The current version is capable of handling a bilateral fault in a homogeneous medium. Our initial set of calculations is designed to understand the importance of plastic material behavior in the fault zone and to determine the scaling of the radiation field with the fault parameters.

Two calculations have been successfully completed. Both are for a 3 km x 3 km bilateral fault in a wholespace. In one case the material behavior is linear elastic. In the other case plastic yielding is allowed in the vicinity of the fault plane.

Detailed analysis of the linear elastic calculation has been completed and excellent results were obtained. The far-field radiation was computed with two methods. One method is to use dislocation theory with the computed slip time histories on the fault. The second method is to expand the outgoing wave field in spherical harmonics (multiple coefficients). Only the latter is formally correct when nonlinear material behavior is allowed near the fault.

The second (nonlinear) earthquake simulation is now being analyzed the same way as the first and results from the two are being compared. A detailed report describing this work is being written.

B. Representation Theorem for Analytic Continuation of Finite Difference Source Calculations

This work is summarized in Section 1.4 and described in detail in Section III.

c. Source Calculations

This work is summarized in Section 1.5 and described in detail in Section IV.

Data Analysis

A. Discrimination Experiment

This work is summarized in Section 1.3 and described in detail in Section II.

B. Development of Spectral m_b and M_s

The Variable Frequency Magnitude (VFM) discriminant being applied in the discrimination experiment (see Section II) is based on the use of narrow band filter magnitudes, called $\bar{m}_b(f)$. These magnitudes reflect the amplitude of the arriving energy at a particular period and a particular arrival time. In essence, they represent the spectral energy of a specific phase arrival. We have long recognized that measurements of this kind might provide a more convenient, stable and reliable signal amplitude indicator than the conventional m_b .

A set of HNME recordings of eleven Pahute Mesa recordings was provided in digital form and is being examined to test the utility of the $\bar{m}_b(f)$. A similar value, $\bar{M}_s(f)$, is defined for the surface waves. Single frequency values are no improvement on the conventional time domain magnitudes. However, $m_b(f)$ and $M_s(f)$ values defined by averaging the $\bar{m}_b(f)$ and $\bar{M}_s(f)$ over a frequency band are very attractive in terms of such qualities as the scatter when plotted versus yield. We are continuing to evaluate this measurement and will report the results to VSC in the near future.

Surface Waves

A. Surface Wave Amplitudes of NTS Explosions Recorded at ALQ and TUC

A special topical report describing this work has been submitted to VSC. The abstract of this report is reprinted below. A classified report with detailed tabulations of the important results has also been prepared and will be submitted to VSC in the near future.

"Source Amplitudes of NTS Explosions Inferred from Rayleigh Waves at Albuquerque and Tucson," by T. C. Bache, W. L. Rodi and B. F. Mason.

Abstract

Comparing observed and synthetic seismograms, source amplitudes of NTS explosions are inferred from Rayleigh wave recordings from the WWSSN stations at Albuquerque, New Mexico (ALQ) and Tucson, Arizona (TUC). The potential influence of source complexities, particularly surface spallation and related phenomena, is studied in detail.

As described in earlier work by Bache, Rodi and Harkrider, the earth models used in computing the synthetic seismograms were inverted from observations at ALQ and TUC. The agreement of observed and synthetic seismograms is quite good and is sensitive to important features of the source.

The events studied are in three distinct areas, Yucca Flat, Pahute Mesa and PILEDRIVER in Climax Stock granite. All events were below the water table and the yields varied from 40 to 200 KT. Within each group the mean static value of the reduced displacement potential (Ψ_{∞}) was determined at a fixed scaled yield, assuming a spherically symmetric point source. The source is then modified to study the effect of: (1) the addition of a double-couple component; (2) the addition of a surface impulse associated with impact of the material spalled from the surface; (3) loss of energy from the free surface reflected waves due to spallation. Comparing observed and synthetic seismograms, the extent of the effect of these secondary phenomena is outlined.

For Yucca Flat and Pahute Mesa events the inferred source amplitudes are in general agreement with values obtained by other methods. The spall impulse is too small to be of much importance. More likely to be important, especially for the Pahute Mesa events, is the loss of energy from the upgoing waves. For PILEDRIVER the double-couple and attenuation of upgoing waves dominate the source determination. Correcting for these phenomena, the explosion source level (Ψ_{∞}) is considerably smaller than has usually been supposed.

Body Wave Studies

In the section on "Data Analysis" we mentioned the set of eleven HNME recordings of Pahute Mesa explosions that are being used to test the development of newly defined magnitude measures. These data are also being analyzed with synthetic seismogram methods to isolate the different effects contributing to m_b -log yield and M_s -log yield relations. An important feature of the body wave recordings is a depth-dependent phase that arrives after pP. This may be due to spall slapdown, tectonic release or some other cause.

To facilitate analysis of these seismograms, our body wave synthesis code (GENSRC) has been improved. The current version will compute the far-field body waves for a source consisting of an explosion (specified by a reduced displacement potential) plus a tectonic release component (specified by a double-couple) plus a spall slapdown component (specified by a stress-time history applied to the free surface) in a layered halfspace.

1.3 SUMMARY OF SECTION II: "DISCRIMINATION EXPERIMENT"

During this reporting period we received short-period seismograms in digital format for nine additional Eurasian events, bringing the total number of events in the data set to 28. The event identification study, based on variable frequency magnitude estimates, was expanded to include eight of the stations that have contributed the bulk of the data. In addition, noise corrections were applied to the magnitude estimates at one of the stations (Bluff, Alaska) and this resulted in a significant enhancement in the separation of the earthquake and explosion-like populations. Tentative identifications for the 28 events based on the combined results from the stations analyzed are as follows: earthquakes - events 36, 38, 41, 47, 48, 49, 50, 55 through 62 and 64;

explosion-like 1, 14, 16 through 22, 33, 53; event 63 - mixed identification (possibly deep). The event locations are described in Figure 2.1 and Table 2.1 of Section II. Future analysis will include noise corrections at all the stations and multi-station discrimination.

1.4 SUMMARY OF SECTION III: "SURFACE WAVE SOLUTION FOR THE ELASTIC EQUIVALENT OF A COMPLEX AXISYMMETRIC SOURCE"

An important problem in computing theoretical seismograms for complex deterministic source models is the linking of finite difference numerical source models with analytical methods for propagating elastic waves in realistic earth models. In Section III we outline the mathematical development of a method to analytically continue the stress waves from an axisymmetric source into a layered earth model for computation of far-field surface waves. The method presented allows for computation of Rayleigh wave motion given the Fourier transformed displacements and stresses monitored on the edge of a cylinder surrounding the source region. Though the resulting expressions appear complicated, they have an asymptotic form which should make interpretation straightforward. The surface wave methods presented here together with the body wave methods presented in an earlier report will allow efficient computation of theoretical seismograms at nearly all distances of interest.

1.5 SUMMARY OF SECTION IV: "SOURCE CALCULATIONS"

As a prelude to our two-dimensional source calculations, we have initiated a review of our one-dimensional spherically symmetric source calculations in order to update and improve our nonlinear constitutive models while ensuring that they are compatible with our two-dimensional codes. The three most important modeling improvements are: (1) the implementation of good equations of state for the cavity gases for salt,

granite and tuff; (2) improvements which make the overburden pressure treatment consistent with our equation of state, and (3) the development of a better effective stress law to model the influence of water saturation in rocks. In Section IV, we present discussions of our latest one-dimensional calculations for PILEDRIIVER (granite), SALMON (salt) and Rainier Mesa saturated tuff, and discuss the modeling improvements made for each.

We are unable to match the SALMON reduced displacement potential (RDP) with the new models using laboratory data for the failure envelope. The calculations give the measured cavity radius, but too small an RDP. We will now attempt to calculate this event in two-dimensions to study the influence of in situ stress in the RDP. If in situ stress proves not to be the explanation of our low calculated RDP, we plan to include viscoelastic effects in the constitutive model for salt. Our calculations for PILEDRIIVER and for saturated tuff were in good agreement with both near and far field data.

II. DISCRIMINATION EXPERIMENT

2.1 INTRODUCTION

Our objective in the discrimination experiment is to analyze seismic waveforms from a large population of events in order to identify these events as either earthquakes or explosions. The waveforms that we are concentrating on are short-period P waves recorded by a global network of seismograph stations. In this section of the report we will summarize the work that has been performed to date.

2.2 DESCRIPTION OF DATA

As of the end of this reporting period we had received short-period digitally recorded seismograms for 28 Eurasian events recorded at one or more of a network of 20 globally distributed seismograph stations. The event locations are indicated in Figure 2.1 by the solid circles and the event dates, origin times and epicentral coordinates, as supplied by Teledyne Geotech, are listed in Table 2.1. With the increase in the number of events in the data base, several concentrations of activity have become apparent. The most active region is the Kuril and Kamchatka Islands which accounts for nearly one-half of the available events. The locations of the eight Eurasian seismograph stations providing data for this experiment are indicated by the solid triangles in Figure 2.1.

The status of the data base as of June 30, 1978 is described in Table 2.2 on a station-by-station basis for each of the 28 events. As can be seen, the number of station seismograms is highly variable from event to event, ranging from two stations for event 36 to twelve stations for events 20 and 53. To date no short-period seismograms have been

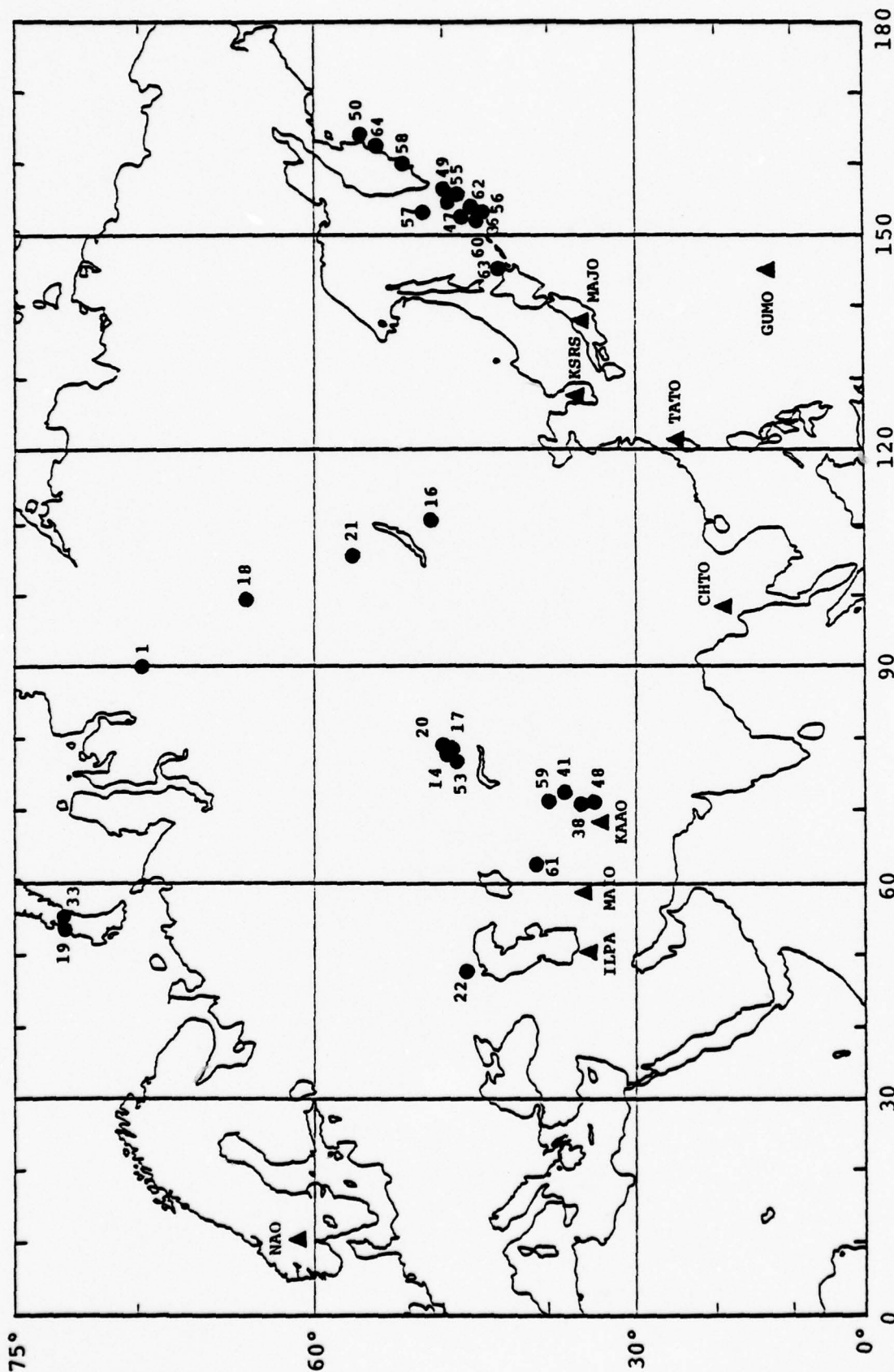


Figure 2.1. Map of Eurasia showing locations of events (solid circles) and several of the stations (solid triangles) included in the discrimination experiment.

TABLE 2.1
EVENT LOCATION INFORMATION

Event Number	Date Yr Mo Dy	Origin Time Hr:Mn:Sec	Coordinates	
			Latitude (°N)	Longitude (°E)
1	77 07 26	16:59:59.9	69.4	90.4
14	77 07 30	01:56:59.9	49.7	78.2
16	77 08 10	22:00:00.7	50.9	111.0
17	77 08 17	04:26:59.8	49.8	78.2
18	77 08 20	22:00:00.6	64.1	99.8
19	77 09 01	03:00:00	73.0	54.0
20	77 09 05	03:03:00	50.0	78.9
21	77 09 10	16:00:00	57.0	106.0
22	77 09 30	06:59:00	48.0	48.0
33	77 10 09	11:00:00	73.0	55.0
36*	77 10 16	20:03:35	48.4	152.9
38	77 10 16	15:02:49	36.9	71.5
41	77 10 13	20:38:42	38.1	72.8
47	77 10 16	21:05:35	49.7	155.1
48	77 10 19	05:02:00	36.3	71.3
49	77 10 19	21:20:37	49.5	155.4
50	77 10 20	08:18:04	56.3	164.1
53	77 10 29	03:07:00	49.0	78.0
55	77 10 26	05:38:52	49.0	155.8
56	77 10 26	07:11:31.3	46.4	153.5
57	77 10 26	13:14:30.9	51.5	153.4
58	77 10 27	07:20:28.9	53.5	160.0
59	77 10 28	21:15:11	39.8	71.9
60	77 10 29	04:14:56.5	47.0	152.3
61	77 10 29	06:26:42.5	41.0	63.7
62	77 10 29	10:33:59.4	47.3	153.1
63	77 10 30	21:38:15.6	44.8	145.0
64	77 10 31	09:40:03.5	55.8	162.7

*Alaska Data Only

TABLE 2.2

STATUS OF DATA BASE: JUNE 30, 1978

EVENT NUMBER	STATION CODE:																			
	000	005	010	015	020	025	030	035	040	045	050	055	080	085	090	095	100	105	110	115
	ANMO	BOCO	CHTO	CTAO	GUMO	KNAO	MAIO	MAJO	NMAO	SNZO	TATO	ZOBO	LAO	NAO	ALK	ATTU	ILPA	KSRS	RK-ON	HN-ME
1	X		X			X	X	X							X			X		
14	X		X			X	X								X			X		
16	X					X						X		X	X			X		
17						X								X	X			X		
18	X		X			X							X				X	X		
19	X		X			X	X	X					X				X	X		X
20	X		X	X		X			X			X			X		X	X		X
21	X			X		X									X		X	X		X
22	X				X	X						X					X	X		X
33									X				X	X	X		X	X		X
36																				
38					X								X	X	X		X	X		X
41						X												X		
47	X		X			X						X	X	X	X	X	X	X		
48						X					X		X	X			X	X		
49	X		X	X	X	X			X				X	X			X	X		
50	X					X		X					X	X	X	X		X		
53	X			X		X	X	X		X			X	X	X	X	X	X		X
55					X								X	X	X	X	X	X		
56				X		X							X	X	X	X	X	X		
57						X					X		X	X	X		X	X		
58															X	X	X	X		
59	X					X	X						X				X	X		
60													X	X	X	X		X		
61						X	X				X		X	X	X	X		X		
62	X												X	X	X	X		X		
63	X					X	X	X					X	X	X	X	X	X		
64	X				X	X							X	X	X	X	X	X		

received from the stations BOCO and SNZO, SRO stations in Columbia and New Zealand, respectively. In addition, while seismograms from the station KSRS are available for 27 of the 28 events in the data base, the extremely high level of background noise prevailing at that site has resulted in seismograms that are dominated by noise for the majority of events. In the following subsection of this report we will describe the discrimination results obtained to date at several of the stations.

2.3 DISCRIMINATION RESULTS

As described in the last quarterly report written under this contract (Rodi, et al., 1978), we employ a narrow band filtering procedure to compute estimates of body wave magnitudes, $\bar{m}_b(f)$, at several different frequencies within the teleseismic bandpass (e.g., 0.3 to several Hertz). By comparing low frequency magnitude estimates with high frequency estimates we can test for event discrimination using short-period P waves recorded at the different stations.

Figure 2.2a shows a seismogram for a short-period P wave from event 47 recorded at the station in Bluff, Alaska (BFAK). The signal is preceded by approximately 30 seconds of background noise. The key feature of the signal analysis procedure we employ is the use of narrow band filters to decompose a time series consisting of signal plus noise, such as that in Figure 2.2a, into a set of quasi-harmonic modulated signals. The modulation or envelope function is calculated by means of the Hilbert transform with the maximum of the envelope function occurring at the group arrival time (t_g) of energy at the center frequency (f_c) of a particular filter. The amplitude of the envelope function is proportional to the spectral amplitude of the filtered signal. The Gaussian-shaped narrow band filters ensure optimal time and frequency domain resolution within the constraints imposed by the sampling theorem or uncertainty principle.

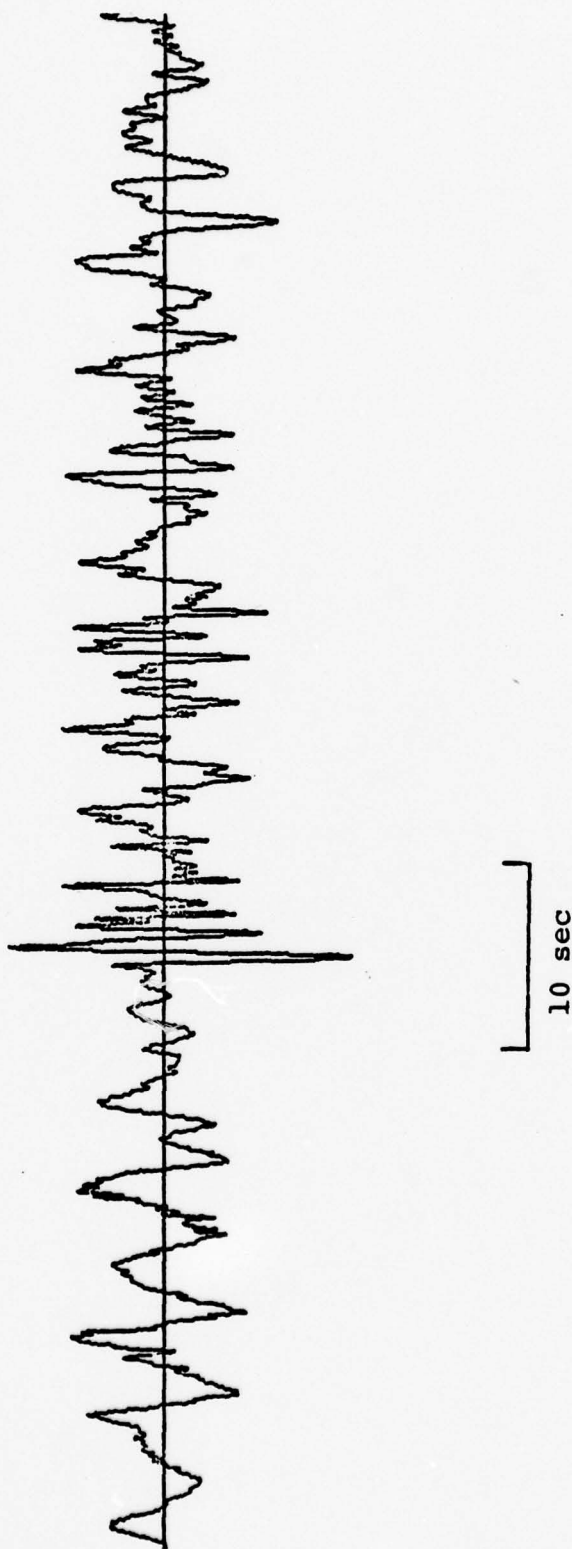


Figure 2.2a. Short-period seismogram for the P wave recorded at Bluff, Alaska (BFAK) from event 47.

Figure 2.2b shows the t_g versus f_c representation of the time series in Figure 2.2a. The envelope peaks from 20 narrow band filters, ranging from 0.4 Hz to 5.0 Hz, are scaled according to their relative amplitudes. For instance, in the case of the filter center frequency $f_c = 2.75$ Hz the scheme for labeling the peaks occurring between $t_g = 402.7$ and 406.9 seconds (after event origin time) is that * corresponds to the maximum amplitude, 9 to an amplitude between 90 and < 100 percent of * and 8 to an amplitude between 80 and < 90 percent of *. The arrival of an undispersed P wave signal will appear as a horizontal alignment of large amplitude peaks in this plane. The prominence of the arrival depends on the ratio of the signal-to-noise spectral amplitude over the frequency band of interest. In Figure 2.2b an undispersed arrival, corresponding to the P wave in Figure 2.2a, is observed at a t_g of approximately 403 seconds over the frequency band 0.5 Hz to 2.75 Hz. Note that the uncertainty in the t_g estimates, Δt_g , is given by $\Delta t_g \geq \frac{1}{4\pi} Q/f_c$; where $\Delta f/f = Q^{-1}$, Δf is the half-width of the narrow band filter at half power and $Q = 10$. Thus, the uncertainty in the group arrival times Δt_g , increases with decreasing filter center frequency.

The envelope peaks occurring at times earlier than $\bar{t}_g^P - \alpha \Delta t_g$, where \bar{t}_g^P is an average group arrival time for the P wave computed over a frequency band corresponding to an acceptable signal-to-noise ratio and α is a parameter > 1 , give estimates of the background noise and can be used to "correct" the signal peaks used for $\bar{m}_b(f)$ discrimination tests. While not evident in Figure 2.2b, later arrivals ($t_g > \bar{t}_g^P + \alpha \Delta t_g$) could be identified with this procedure. In Figure 2.2c the sum of the amplitudes of the envelope peaks at the 20 different frequencies is plotted as a function of time. This plot indicates the ratio of signal amplitude to the noise or later arrivals.

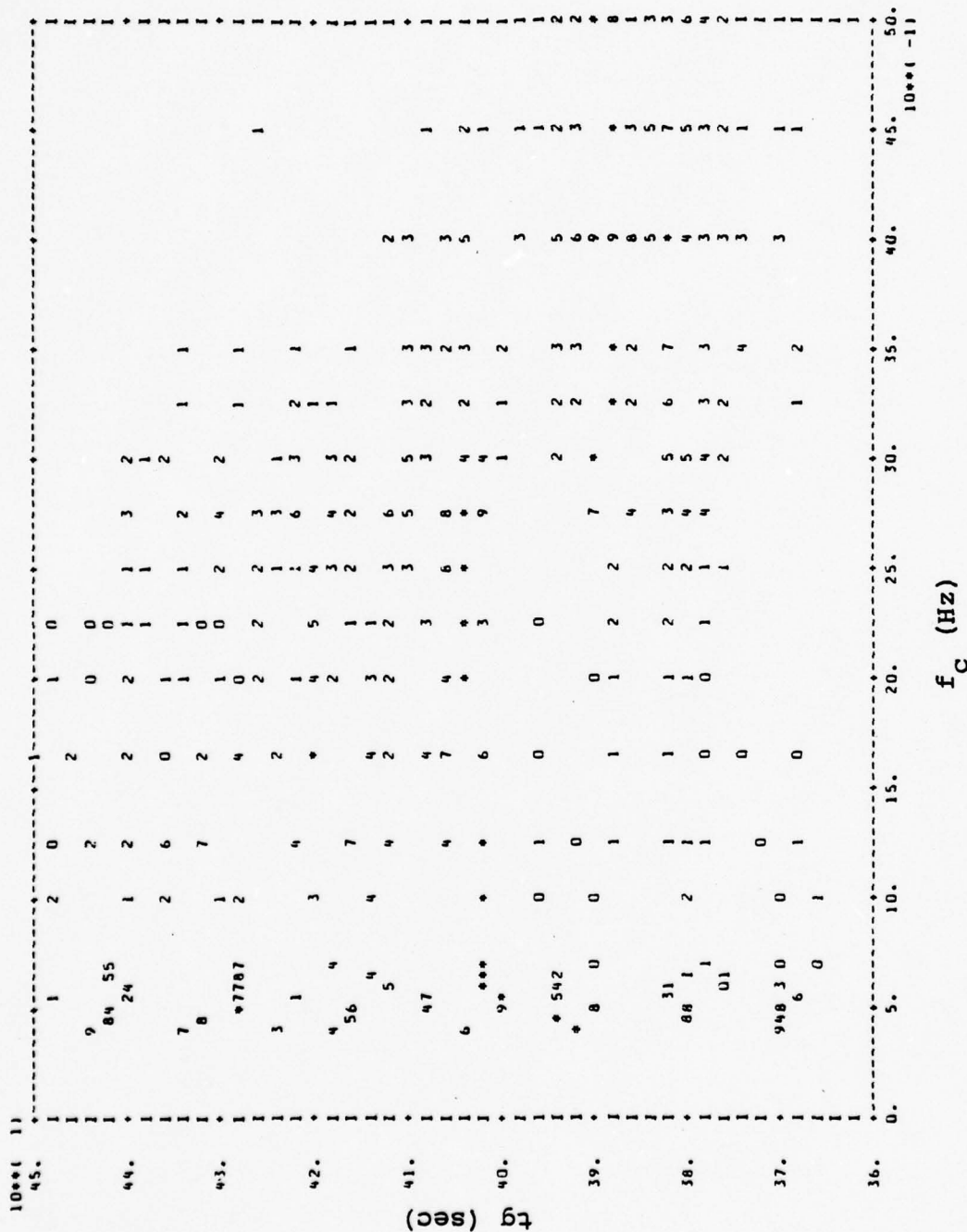


Figure 2.2b. Group arrival time (t_g) as a function of filter center frequency (f_c) for event 47 recorded at Bluff, Alaska (BFAK).

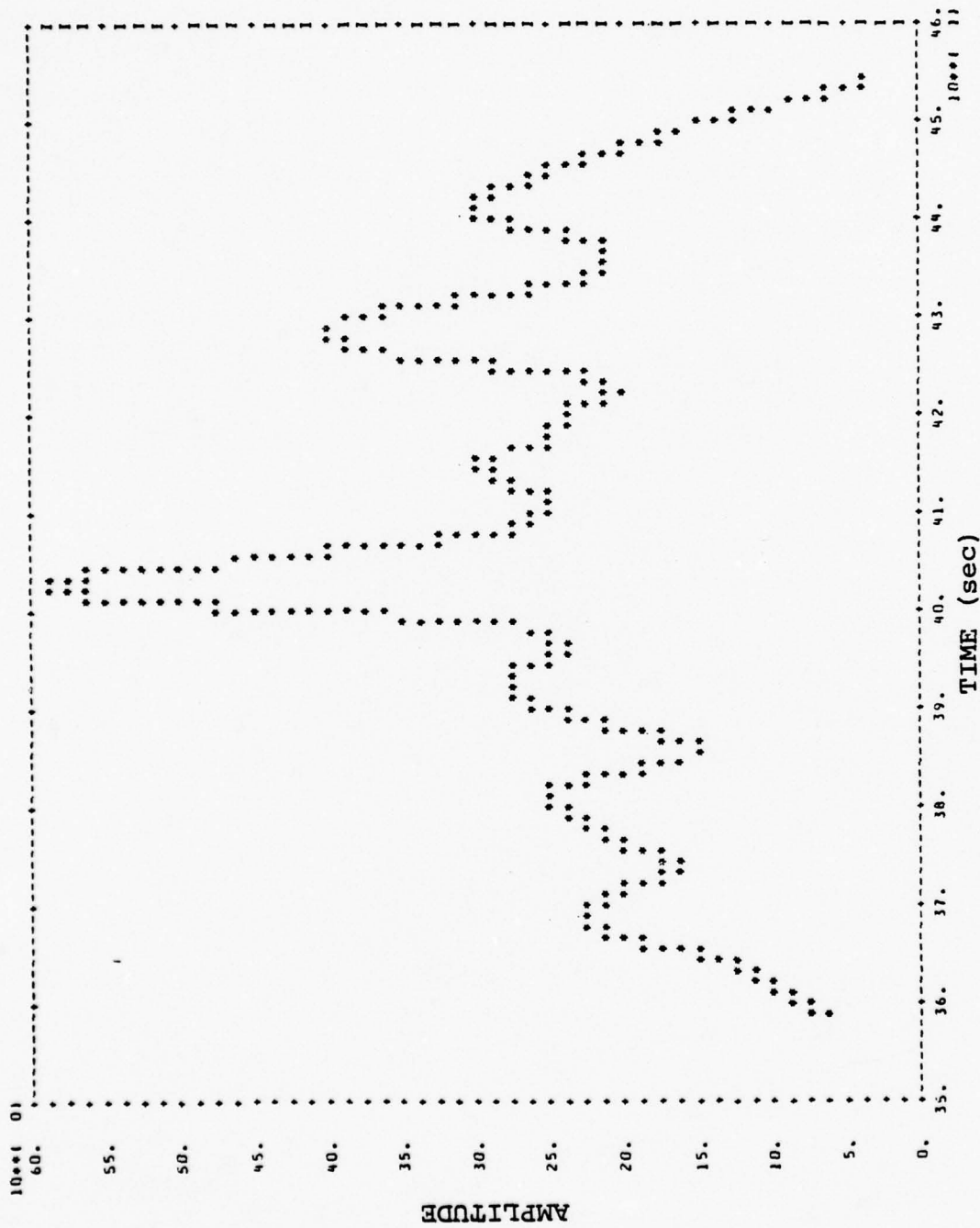


Figure 2.2c. Sum of the envelope amplitudes plotted as a function of time after origin time for event 47 recorded at Bluff, Alaska (BFAK).

Figures 2.3a, 2.3b and 2.3c are a similar sequence, that is P wave seismogram, $t_g - f_c$ and sum of envelope peaks, for an event that was previously identified (Rodi, et al., 1978) as being explosion-like. The signal-to-noise ratio for this event as recorded at BFAK is much larger than that for event 47 (e.g., compare Figures 2.2a and 2.3a). As a result, in Figure 2.3b there is a near perfect horizontal alignment of t_g estimates over the entire frequency band, 0.4 Hz to 5.0 Hz, with a mean $\bar{t}_g = 616$ seconds. In Figure 2.3c the sum of the envelope peaks indicates a signal-to-noise ratio for this event of approximately 45.

The procedure for testing for discrimination in the $\bar{m}_b(f)$ plane follows from the above results. Magnitude estimates at several combinations corresponding to peaks with t_g 's within $\bar{t}_g \pm \alpha \Delta t$ are selected for the different events and compared on a station-by-station basis. Plots of $\bar{m}_b(f)$ planes for eight different stations are shown in the following figures. In each of these figures the arrows attached to the closed circles or triangles indicate the principal direction that a noise correction would move the points. The length of an arrow is proportional to this correction.

Figures 2.4a through 2.4c shows $\bar{m}_b(f)$ results for 18 events recorded at Bluff, Alaska (BFAK). The epicentral distances for these events ranges from 25 to 65 degrees. Three different combinations of high and low filter center frequencies are plotted in order to give an indication of the behavior of the event populations. In the previous quarterly report events 1, 14, 16, 17, 21, 33 and 53 were identified as possible explosions. Thus, the lines drawn in these figures mark the boundaries between earthquake and explosion-like events. Comparing these three figures we see very little movement of all the events except 63, and to a less extent events 64 and 16, with no crossings of the population boundaries. The other point to note about the events in all three of these figures is that in

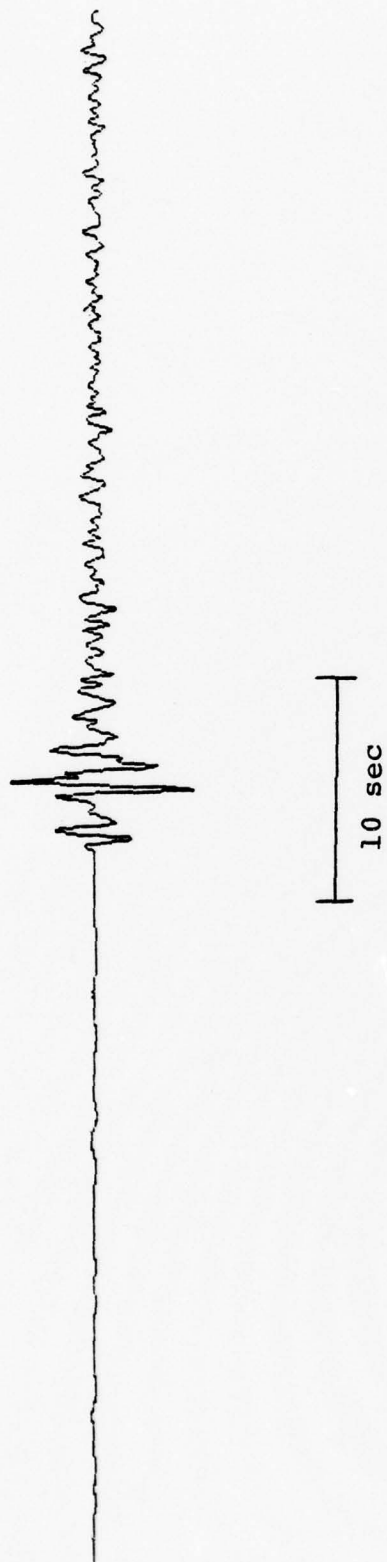


Figure 2.3a. Short-period seismogram of P wave recorded at Bluff, Alaska (BFAK) from event 53.

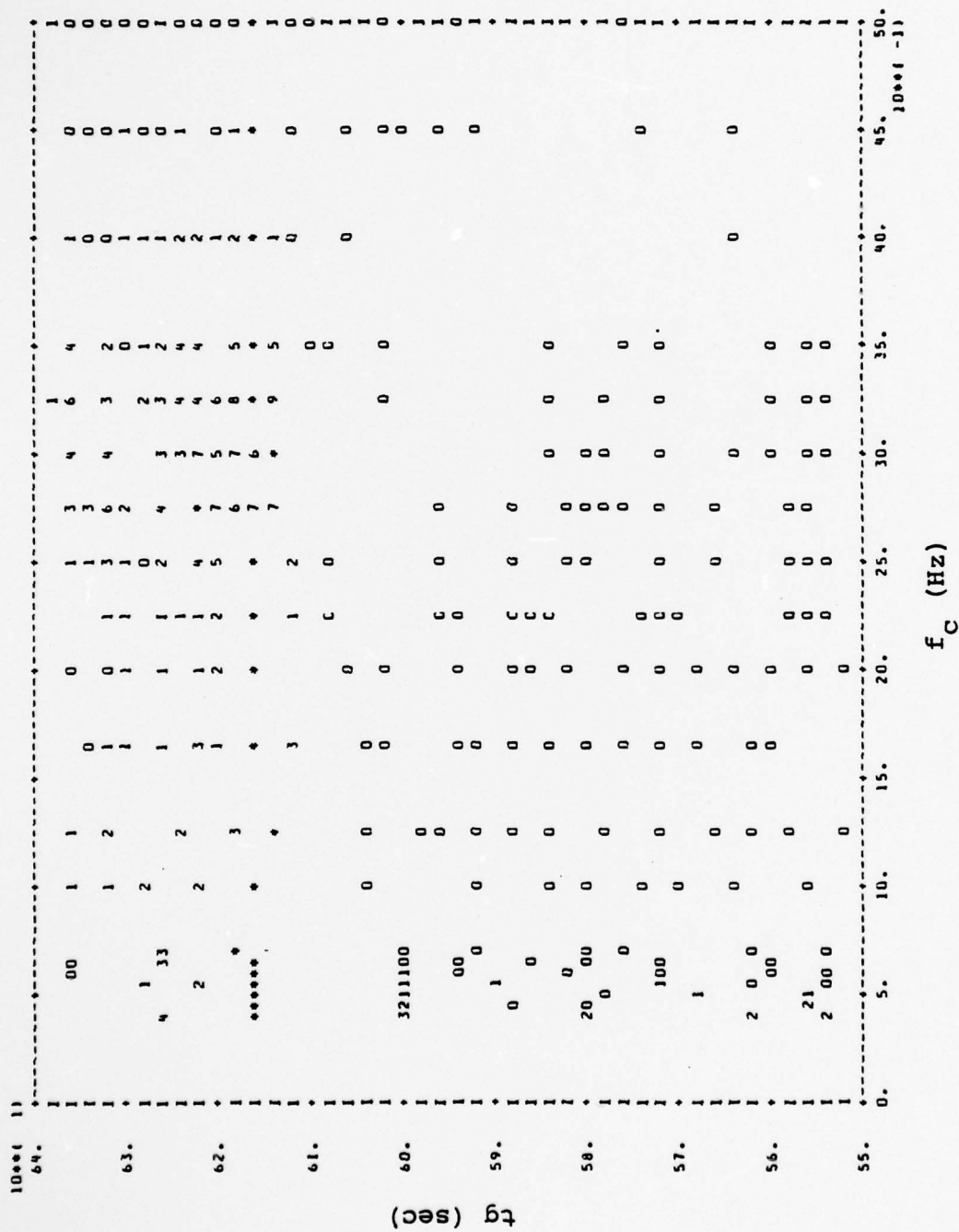


Figure 2.3b. Group arrival time (t_g) as a function of filter center frequency (f_c) for event 53 recorded at Bluff, Alaska (BFAK).

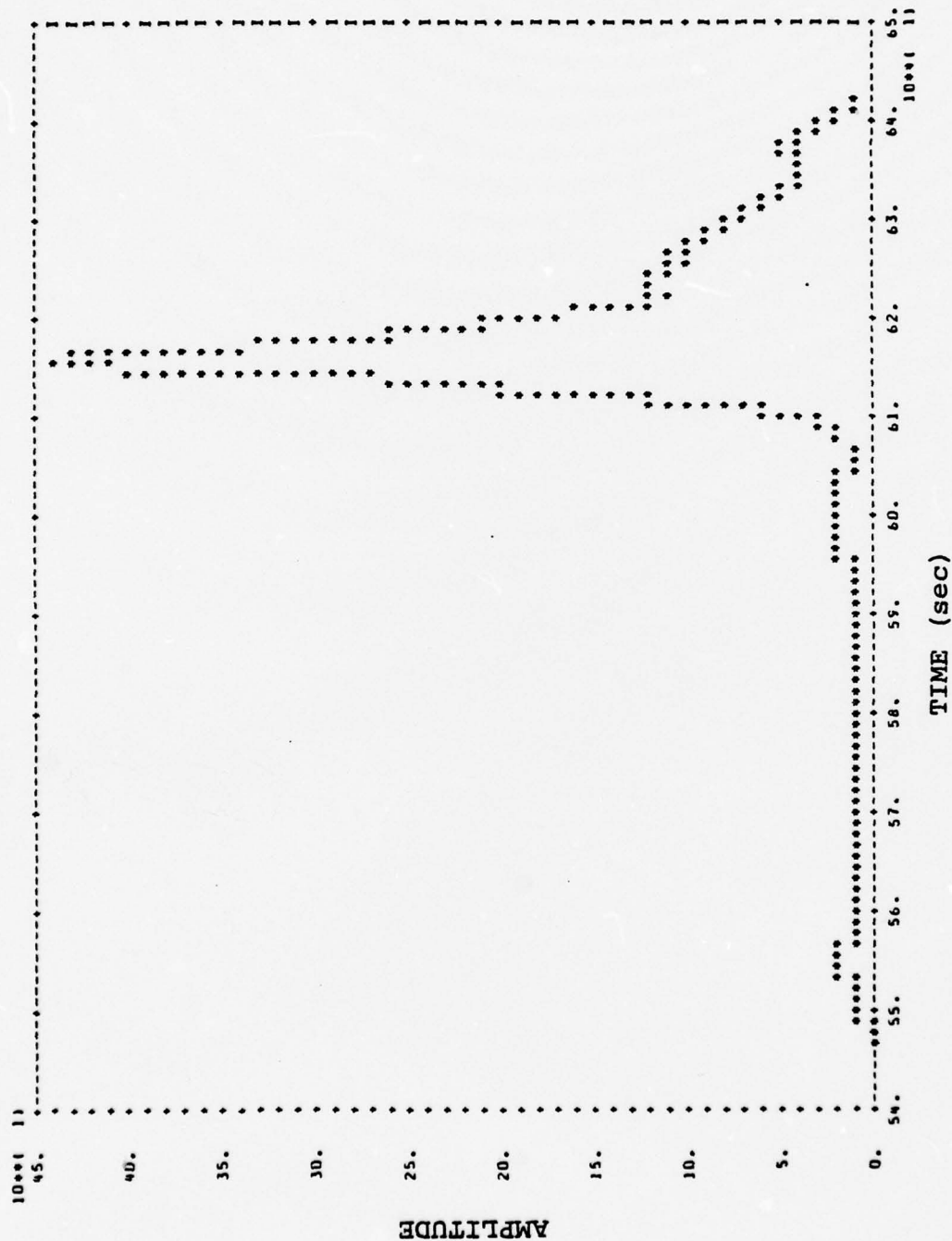


Figure 2.3c. Sum of the envelope amplitudes plotted as a function of time after origin time for event 53 recorded at Bluff, Alaska (BFAK).

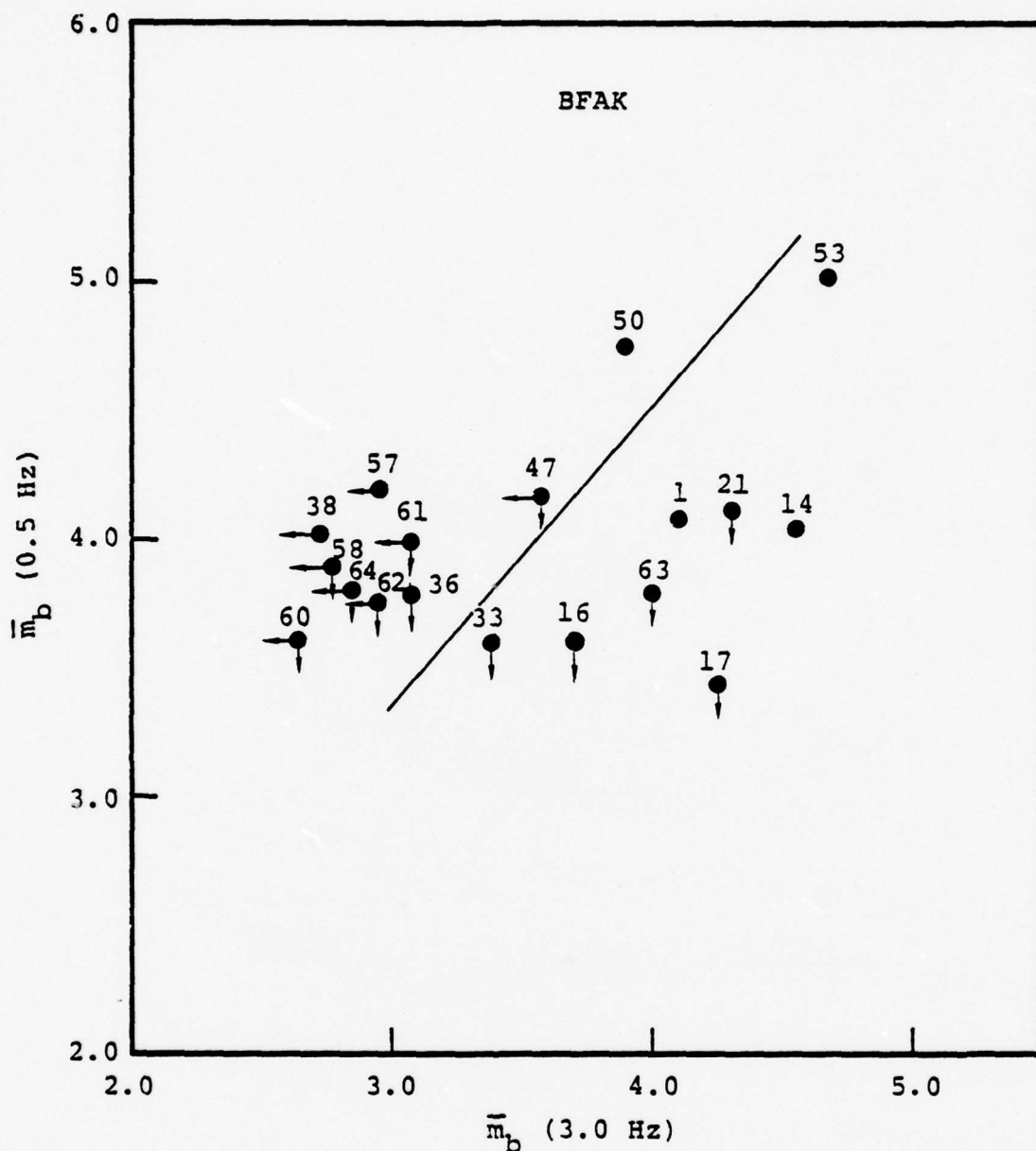


Figure 2.4a. Variable frequency magnitude, $\bar{m}_b(f)$, estimates, not corrected for noise, at $f_c = 0.5 \text{ Hz}$ and 3.0 Hz for events recorded at Bluff, Alaska (BFAK). The arrows indicate the principal directions in which the $\bar{m}_b(f)$ estimates would move when noise corrections are applied. The straight line on this, and subsequent $\bar{m}_b(f)$ plots, marks the approximate boundary between earthquake and explosion-like events.

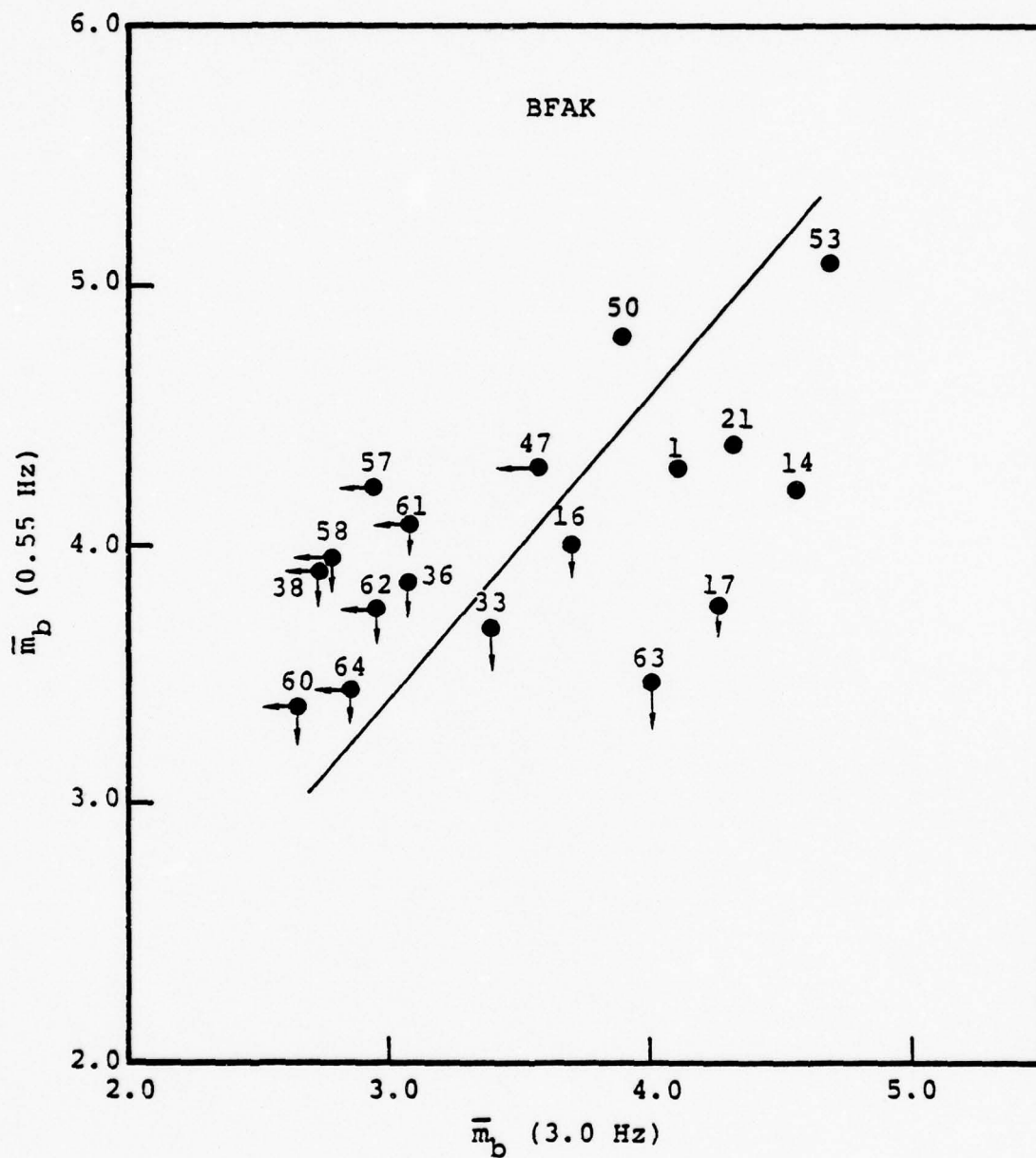


Figure 2.4b. Variable frequency magnitude, $\bar{m}_b(f)$, estimates, not corrected for noise, at 0.55 Hz and 3.0 Hz for events recorded at Bluff, Alaska (BFAK).

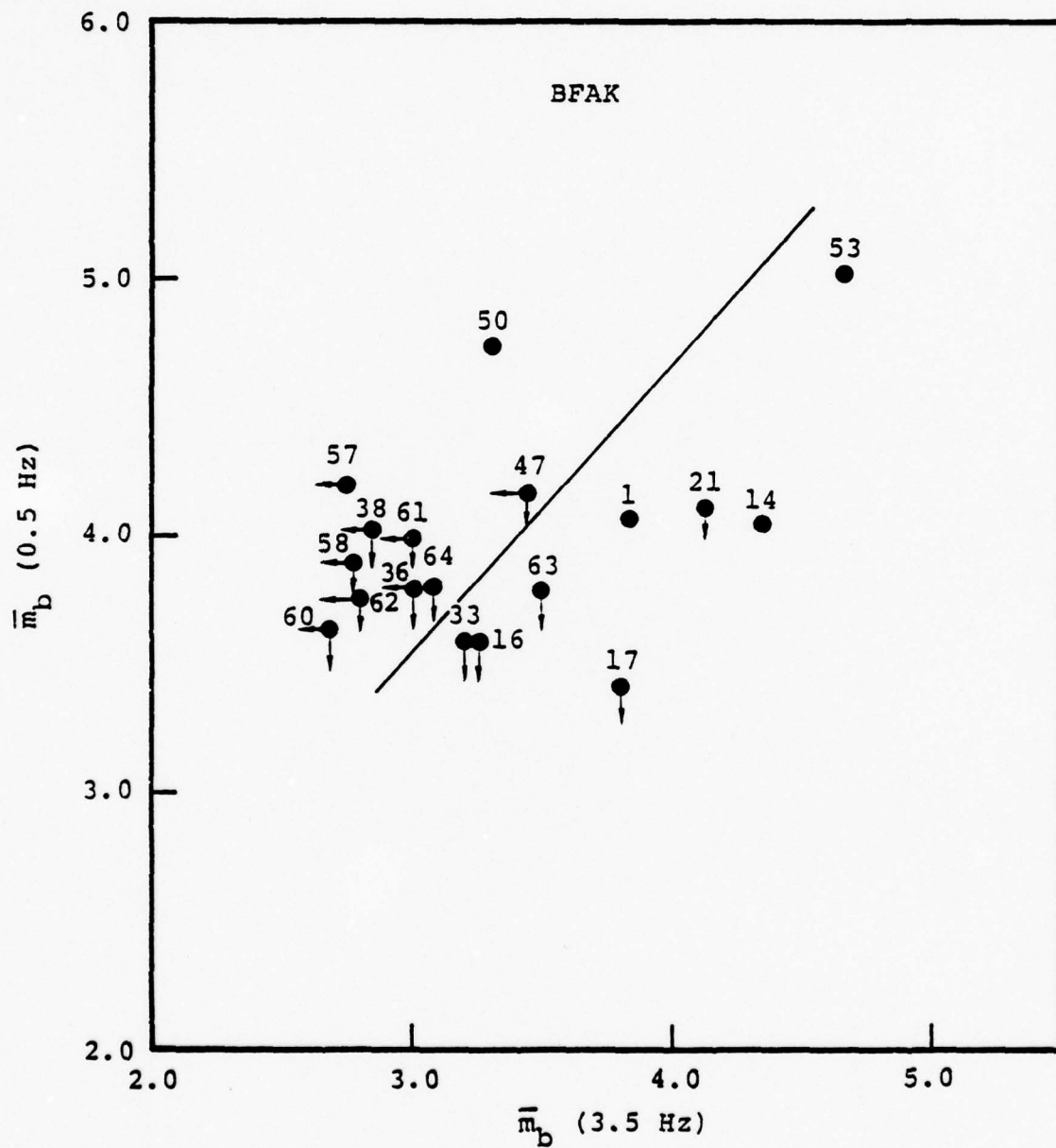


Figure 2.4c. Variable frequency magnitude, $\bar{m}_b(f)$, estimates, not corrected for noise, at 0.5 Hz and 3.5 Hz for events recorded at Bluff, Alaska (BFAK).

general the noise correction required for events in the explosion like population primarily affects the low frequency magnitude estimate. For events in the earthquake population, the required noise correction affects either both the high and low frequency estimates or the high frequency estimate preferentially.

As described above, we would expect the application of noise corrections to increase the separation of the two event populations. To test this we computed mean noise levels for all the explosion-like events (except number 1; no noise segment available) and several of the earthquakes in Figures 2.4a and 2.4b. The means were based on envelope peaks preceding the signal arrivals as noted in Figures 2.2b and 2.3b. The noise estimates were then subtracted from the signal amplitudes at the corresponding frequencies and noise corrected $\bar{m}_b(f)$ values were recomputed. These revised $\bar{m}_b(f)$ estimates are plotted in Figures 2.5a and 2.5b along with population boundary lines. Comparing Figures 2.4 and 2.5 it is immediately apparent that the separation of the event populations has been significantly increased by the application of noise corrections. In addition, there is a definite reduction in the scatter of the explosion-like population.

Figures 2.6 through 2.11 give $\bar{m}_b(f)$ results for several of the stations previously reported on (LASA, ANMO and KAAO) as well as four new ones (ILPA, KSRS, CTAO and CHTO). As of the end of this reporting period no noise corrections had been applied to the events in Figures 2.6 through 2.11. As a result the separation of event populations is not nearly as large as that in Figures 2.5a and 2.5b. Nevertheless, it is still possible to draw some conclusions about many of the events with lower signal-to-noise ratios. Before summarizing the discrimination results there are several points to be noted in particular. First, comparing the results in Figures 2.4 through 2.11, we see that the only well recorded events

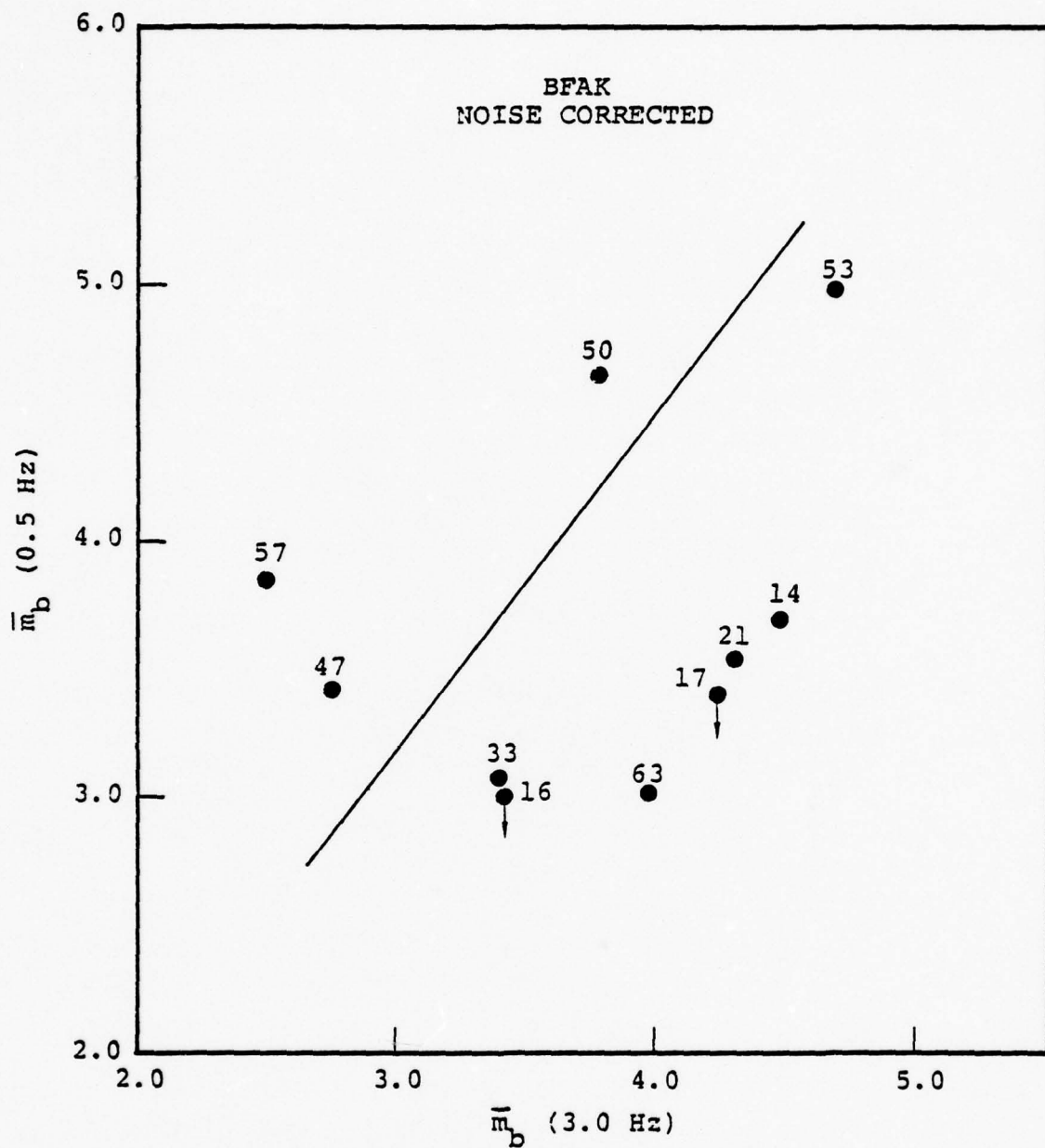


Figure 2.5a. Noise corrected $\bar{m}_b(f)$ estimates for events recorded at BFAK. Compare this figure with Figure 2.4a.

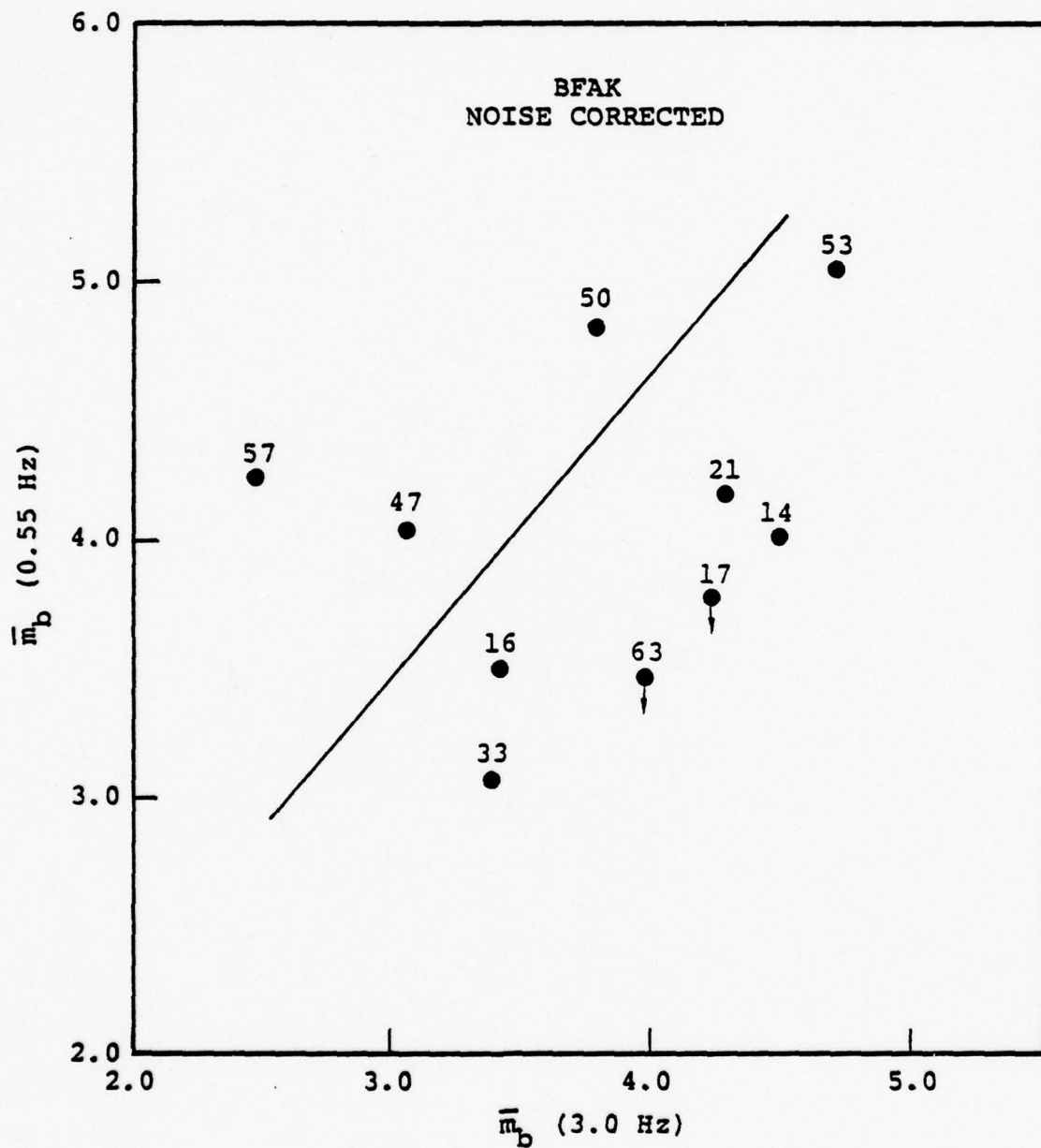


Figure 2.5b. Noise corrected \bar{m}_b (f) estimates for events recorded at BFAK. Compare this figure with Figure 2.4b.

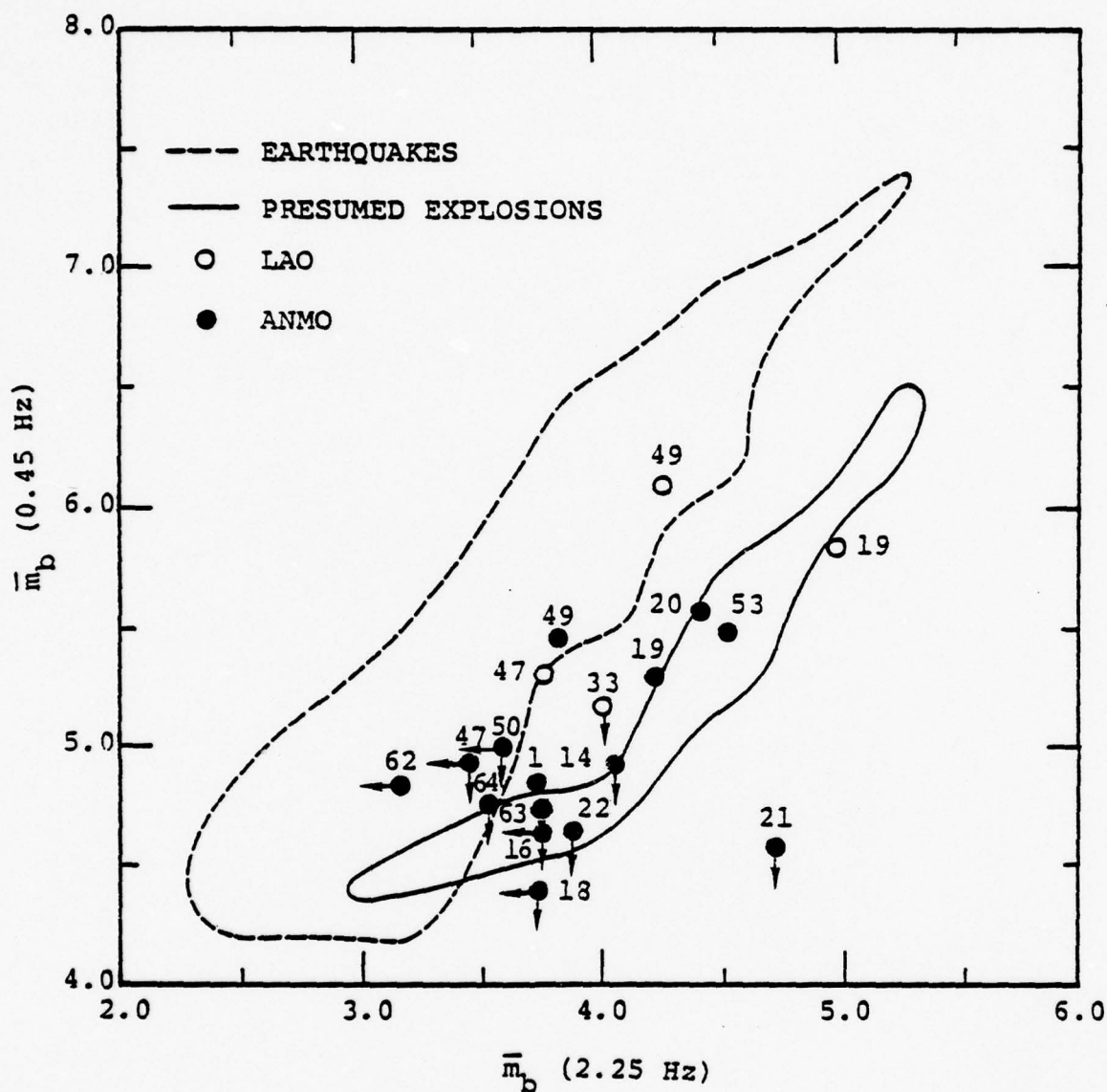


Figure 2.6. Variable frequency magnitude, $\bar{m}_b(f)$, estimates not corrected for noise, at $f_c = 0.45 \text{ Hz}$ and 2.25 Hz based on short-period P waves recorded at ANMO and LAO. These estimates are compared with event populations (dashed and solid lines) previously studied at LASA (see Rodi, *et al.*, 1978).

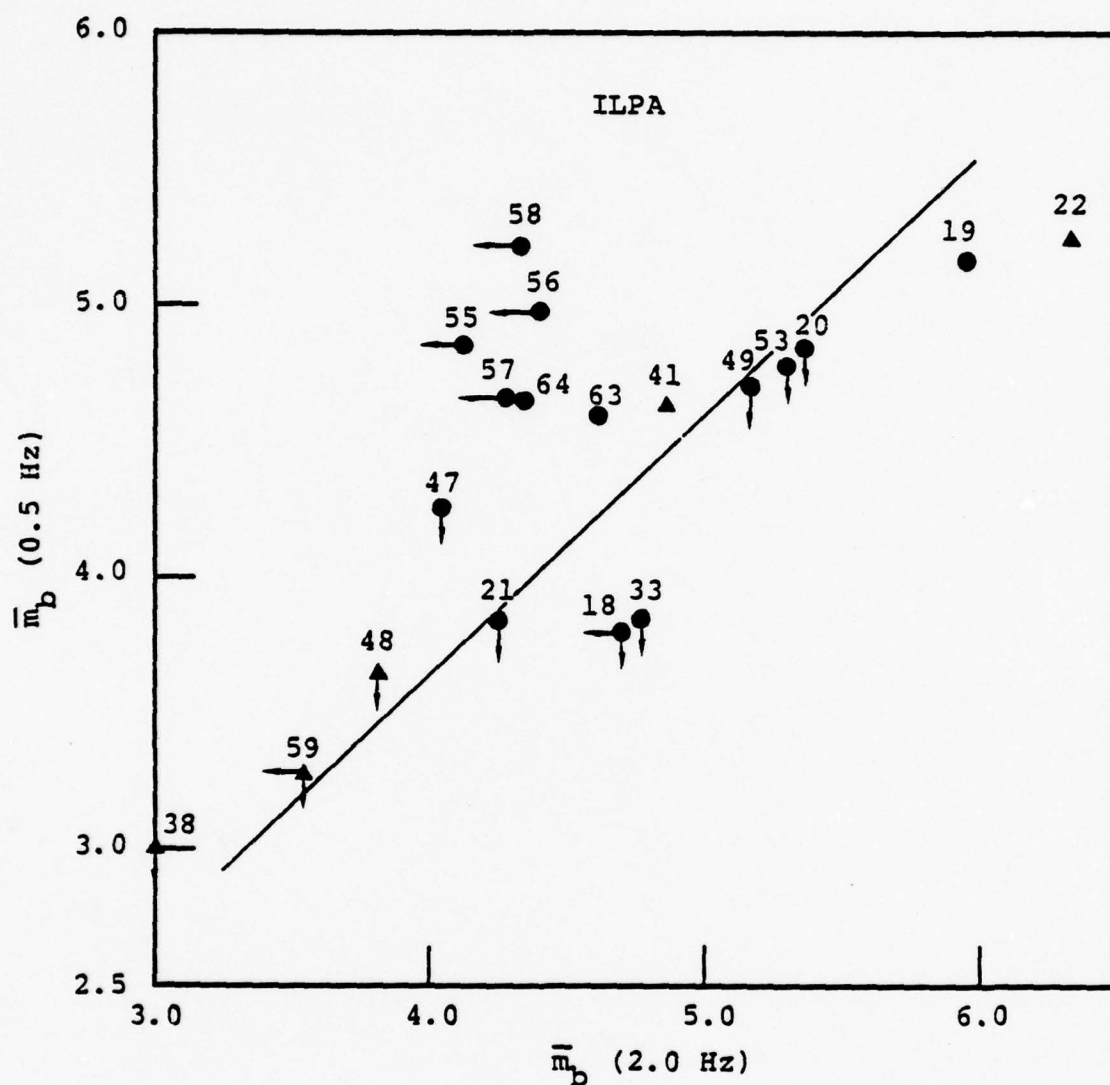


Figure 2.7. Variable frequency magnitude, $\bar{m}_b(f)$, estimates, not corrected for noise, for events recorded at the Iranian array (ILPA).

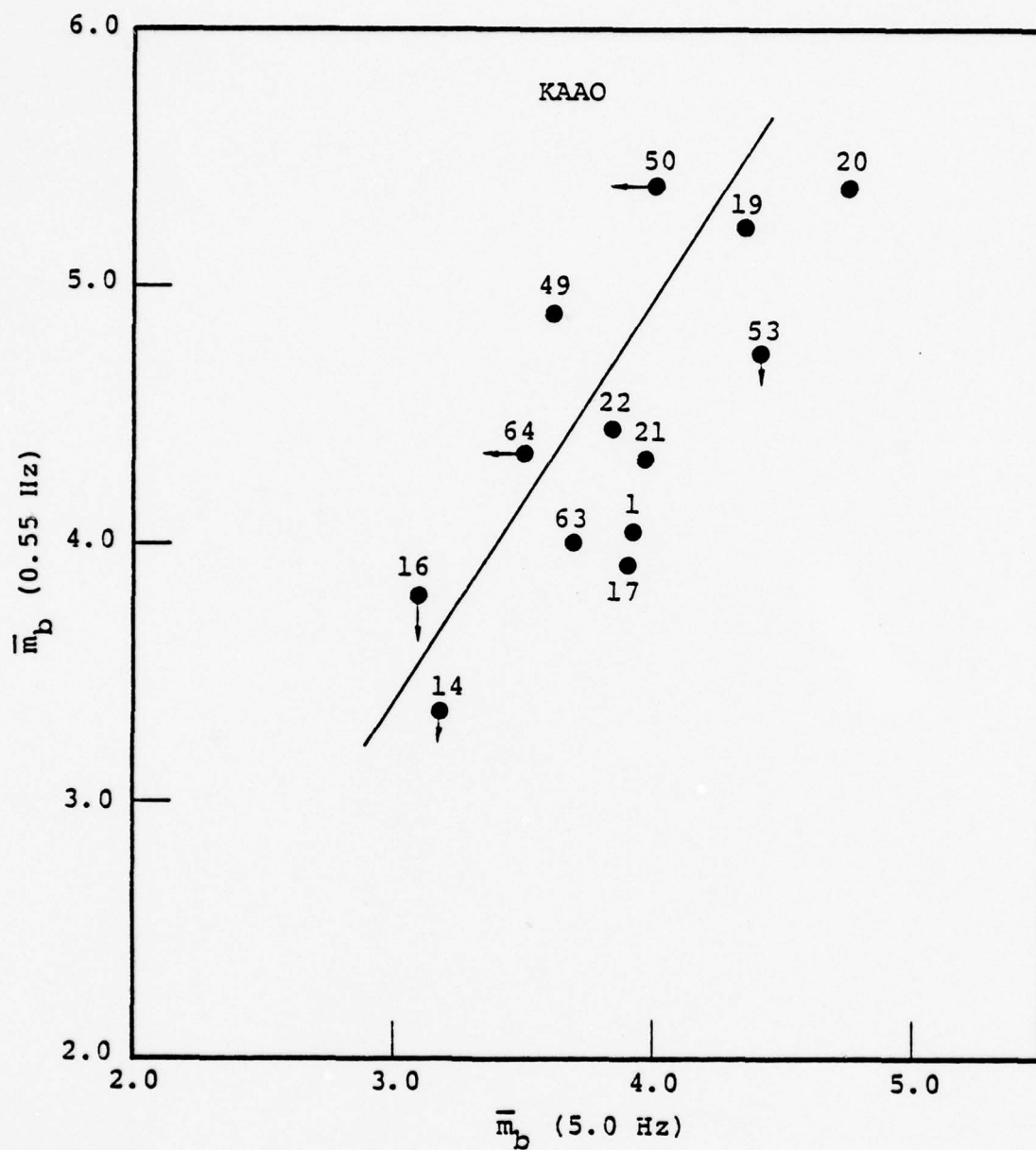


Figure 2.8. Variable frequency magnitude, $\bar{m}_b(f)$, estimates, not corrected for noise, for events recorded at the SRO station in Kabul, Afghanistan (KAAO).

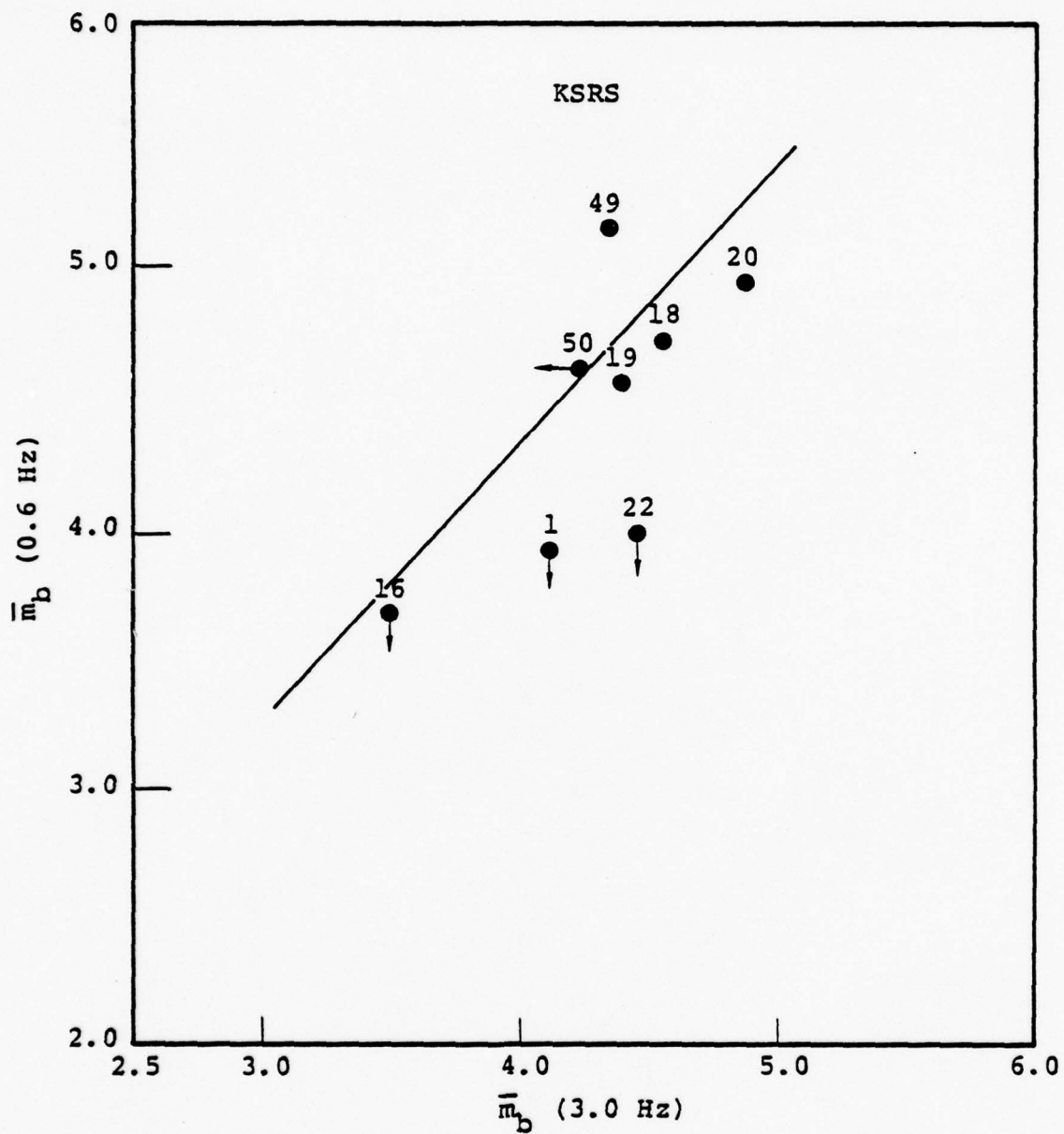


Figure 2.9. Variable frequency magnitude, $\bar{m}_b(f)$, estimates, not corrected for noise, for events recorded at the Korean array (KSRS).

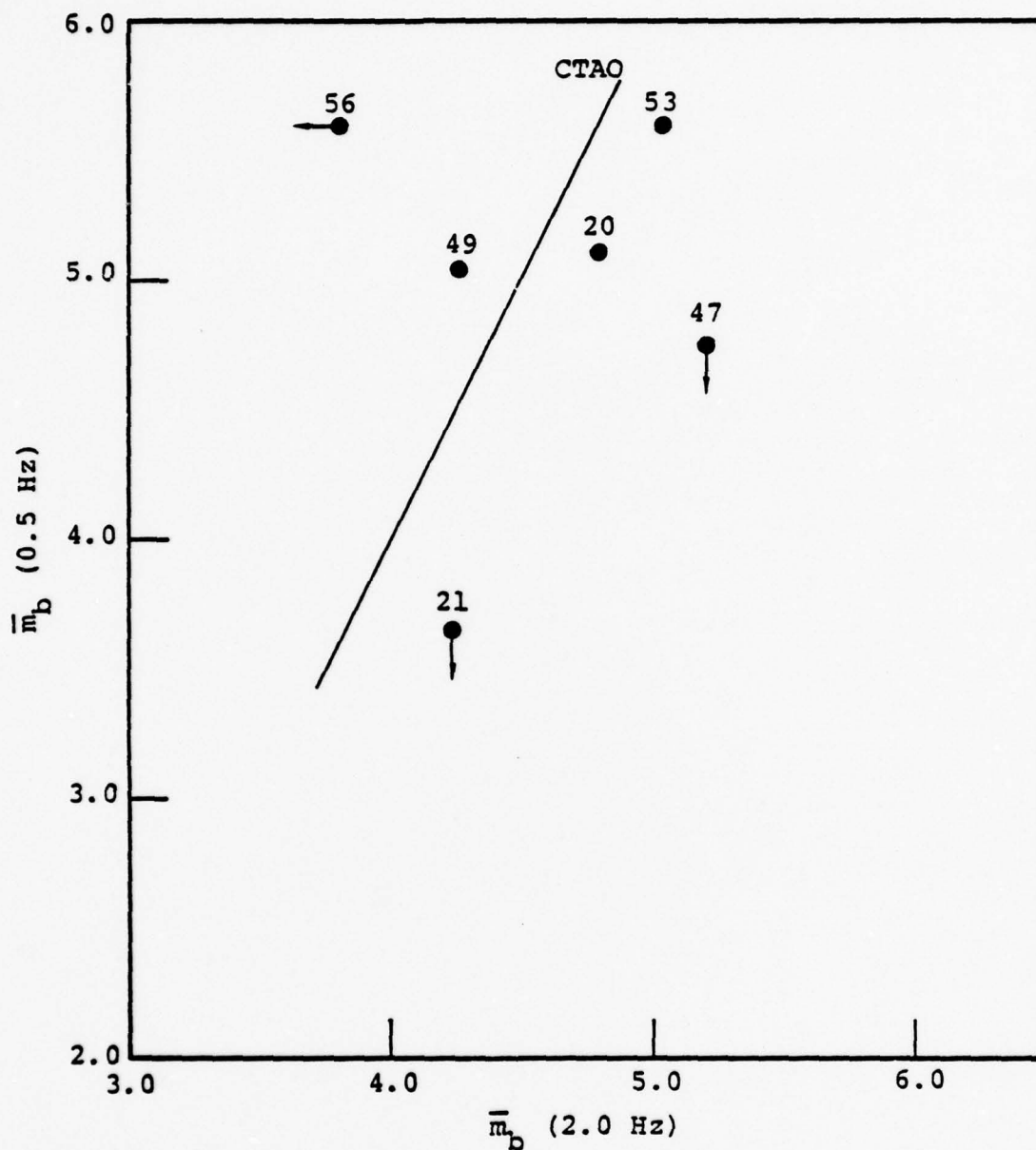


Figure 2.10. Variable frequency magnitude, $\bar{m}_b(f)$, estimates, not corrected for noise, for events recorded at the SRO station in Charters Towers, Australia (CTAO).

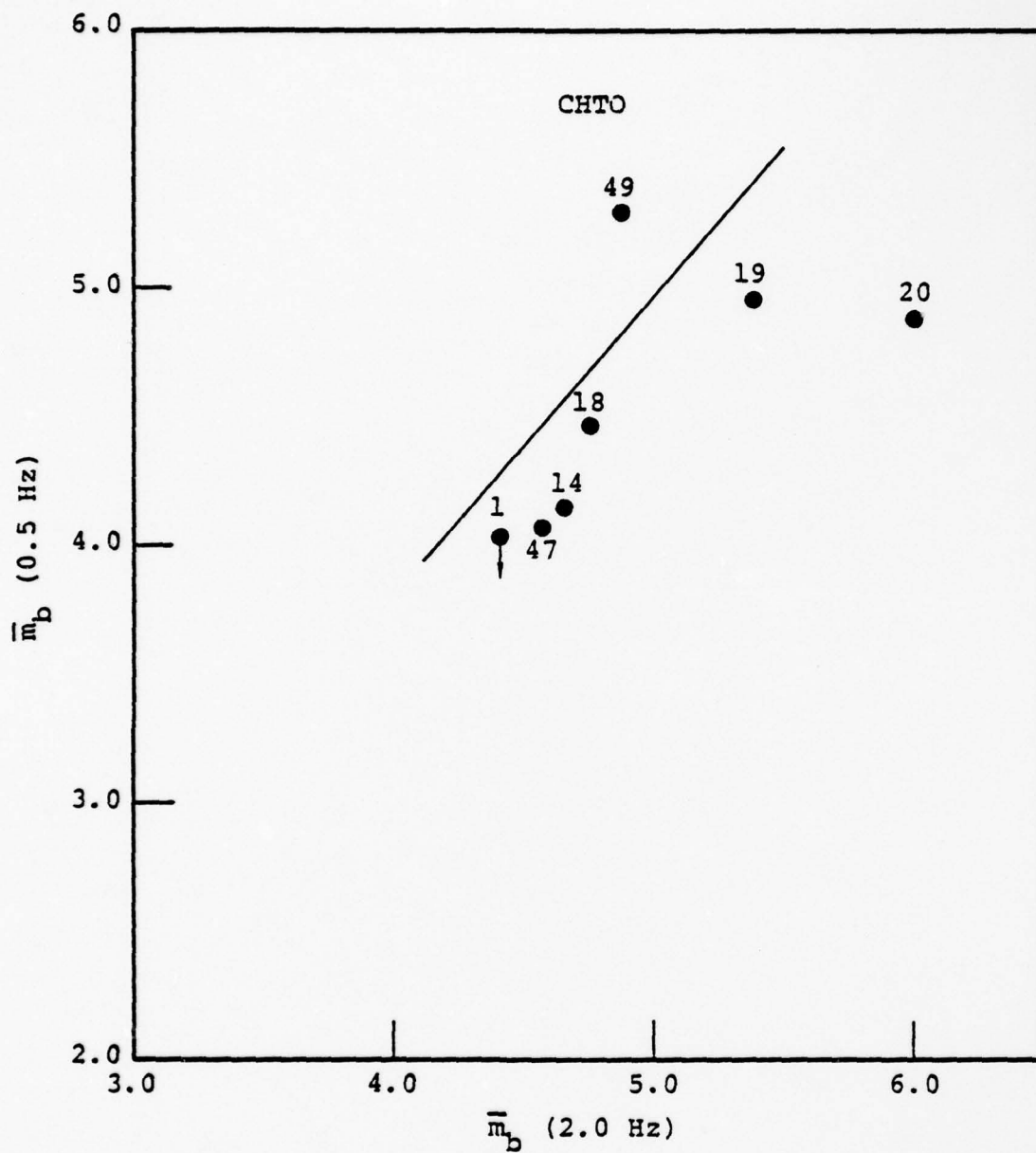


Figure 2.11. Variable frequency magnitude, $\bar{m}_b(f)$, estimates, not corrected for noise, for events recorded at the SRO station in Chaing Mai, Thailand (CHTO).

that cross the population boundaries (i.e., the straight lines) are events that are thought to be earthquakes. For instance, event 63, which occurs landward of the trench off northern Japan plots in with the explosion-like events at stations BFAK, ANMO and KAAO, but plots in the earthquake population at ILPA. Event 47, located in the Kuril Islands, would be identified as an earthquake at LASA, ANMO, BFAK and ILPA, but explosion-like at CTAO and CHTO. On the other hand, in no case does a well recorded explosion-like event cross over into the earthquake populations at any of the stations analyzed.

2.4 SUMMARY

During this reporting period, we received short-period seismograms in digital format for nine additional Eurasian events, bringing the total number of events to 28, and continued with an event identification study based on variable frequency magnitude estimates. Table 2.3 summarizes the preliminary event identifications that have been made to date based on results from eight of the stations contributing data to this experiment. The most important thing to note in this table is the fairly consistent dichotomy of most of the events. Of the three events (47, 49 and 63) which do cross population boundaries, the majority of stations predict that two (47 and 49) are earthquakes and the third (63) explosion-like. The locations of these three events (Figure 2.1) along the Japan and Kuril arcs suggests that they are most likely earthquakes. Thus, it is clear that a multi-station discriminant would improve on the results in Table 2.3. At this point in time, however, with only 28 events in the data base, and fewer than 28 available for any one station (Table 2.3), we cannot define the population statistics that are necessary for a multi-station analysis. Assuming the data base continues to increase at its past rate we should be able to test a multi-station

TABLE 2.3

34

discriminant at KAAO, KSRS, ILPA and the Alaskan stations within the next reporting period.

Our plans for the future are the following:

1. Continue to test for discrimination at all the stations participating in the discrimination experiment.
2. As seen in Figures 2.4a and 2.4b, the application of noise corrections to the $\bar{m}_b(f)$ estimates is essential for optimum discrimination. Thus, during the next time period we will concentrate on correcting the data at all the stations prior to testing for discrimination.
3. Test for multi-station discrimination using a larger event population and noise corrected $\bar{m}_b(f)$ estimates.

III. SURFACE WAVE SOLUTION FOR THE ELASTIC EQUIVALENT OF A COMPLEX AXISYMMETRIC SOURCE

3.1 INTRODUCTION

Rodi, et al. (1978) presented a technique for linking numerical source calculations with analytical techniques for elastic wave propagation. The objective is to analytically continue the source displacement field into an elastic region where motion due to propagating waves can be computed efficiently. The method employs the elastodynamic integral representation theorem of Burridge and Knopoff (1964) which relates the total displacement field inside a given volume to the values of stress and displacement on the surface of the volume. For the specific case of an axisymmetric source, displacements outside the source region can be computed given only stresses and displacements monitored on the edges of a cylinder enclosing the source (which can be obtained from finite difference or finite element calculations) and the point force Green's functions integrated around the cylinder radius (which can be obtained by analytical methods).

The mathematical development of the body wave problem using Cagniard-deHoop inversion techniques is given in Rodi, et al. (1978). Here we deal with the case of surface waves excited in a multilayered elastic or linearly anelastic medium. Though an incomplete description of the motion in a multilayered half-space, the surface wave contributions often can be used effectively to infer source parameters. At regional and teleseismic distances the part of the observed motion due to surface waves can usually be isolated for study (Rodi, et al. (1978)). In certain cases, dominant motion at very close distances may be approximated quite well with a surface wave description (Swanger and Boore (1978)).

The development to follow is quite general; it can be applied to many cases where body wave methods cannot be applied without great difficulty. The elastic region need not be homogeneous in the vicinity of the source region. Plane layer boundaries may intersect the source region where the displacements and stresses are monitored. In theory the method could be applied to continuously varying material properties with depth in the elastic region. For this case there is a practical limitation in that no efficient technique for computation of surface wave dispersion parameters exists for media with continuously varying moduli with depth, though recently, methods have been proposed (Wiggins, 1976). Also, with only minor adjustments in the source related terms, the method could be extended to full wave solutions applied in the Fourier frequency domain (Apsel, et al. (1977)).

3.2 THEORETICAL DEVELOPMENT

Given monitored displacements and stresses in the source region, the surface wave motion can be computed if the Green's functions appropriate to surface wave motion can be applied directly. For the body wave problem, it is most efficient to compute the displacement motion due to one cylinder azimuth and integrate over azimuth numerically. In the surface wave problem we can analytically integrate the Green's functions over azimuth before computing any of the final displacement field. To show this, we begin with the Green's function representation of the displacement field due to a point force. Expressions here may differ slightly from those of Rodi, et al. (1978) because of algebraic errors present in that work and also because of differences in the coordinate system chosen here.

We choose a coordinate system with positive z downward and receiver at a horizontal distance r from the source. Given either a vertical force or a horizontal force in a

direction ϕ from the receiver azimuth at depth z_0 , the Green's tensor components associated with vertical and radial displacements observed at z can be written in the Fourier frequency domain as

$$g_{ij} = \frac{1}{4\pi\rho\omega^2} \int_0^\infty k dk \left[A_{ij}^\alpha(k, \omega) + A_{ij}^\beta(k, \omega) \right] \quad (3.1)$$

where

$$A_{ij}^\alpha = \frac{e^{-v_\alpha |z-z_0|}}{v_\alpha} \begin{bmatrix} -k^2 e^{-i\phi} \frac{dJ_1(kr)}{dkr} & \epsilon k v_\alpha J_1(kr) \\ \epsilon k v_\alpha e^{-i\phi} J_1(kr) & v_\alpha^2 J_0(kr) \end{bmatrix}$$

$$A_{ij}^\beta = \frac{e^{-v_\beta |z-z_0|}}{v_\beta} \begin{bmatrix} \left(v_\beta^2 J_0(kr) - \frac{k^2 J_1(kr)}{kr} \right) e^{-i\phi} & -\epsilon k v_\beta J_1(kr) \\ -\epsilon k v_\beta e^{-i\phi} J_1(kr) & -k^2 J_0(kr) \end{bmatrix}$$

with

$$v_\gamma = \left(k^2 - \frac{\omega^2}{\gamma^2} \right)^{1/2}, \quad \epsilon = \text{sgn}(z-z_0)$$

and only the real part is retained in exponentials involving the azimuth ϕ . The subscripts i, j are interpreted as follows:

- $i=1$ implies horizontal displacement in the $\phi=0$ direction;
- $i=2$ vertical displacement;
- $j=1$ horizontal force in the ϕ direction;
- $j=2$ vertical force.

Since we are dealing with an axisymmetric source, we have not considered the tangential components of displacements. Also, because of the source symmetries, we need only consider the contributions due to Rayleigh waves in calculating surface wave motion. It would seem appropriate to use only the P-SV contributions of the Green's tensor, and not the complete representation of the components of interest as given above. Recent work by Herrmann (1978) has shown that the complete P-SV and SH components of the motion contain non-propagating near-field terms which cancel in the displacement field only when the two systems of motion are considered simultaneously. In the above expressions we have eliminated these terms. The contributions expressed above can still be considered P-SV type motion, but they are not the complete P-SV motion in a formal sense.

To apply the above Green's functions to the equations of Rodi, et al. (1978) directly, we need to evaluate them on the edge of the cylinder surrounding the source region and then integrate over all azimuths. When we displace the point forces from the origin to the cylinder edge, we must modify the angular dependences (Figure 3.1). Given a radial force at cylinder radius a and azimuth ϕ , the effective azimuth to the receiver becomes $\phi + \psi$. Also, the radial sense of motion observed by the receiver will change with ϕ . We are interested in horizontal motion in a fixed radial direction (\vec{e}_r direction), not the effective radial direction for a given ϕ (\vec{e}_R direction). It is clear from Figure 3.1 that the desired contribution for a given ϕ is $\cos\psi$ times the calculated radial displacement. These corrections will be quite small at far-field distance, but, because of the vector summation properties of Bessel functions, they simplify evaluation of the azimuthal integrations.

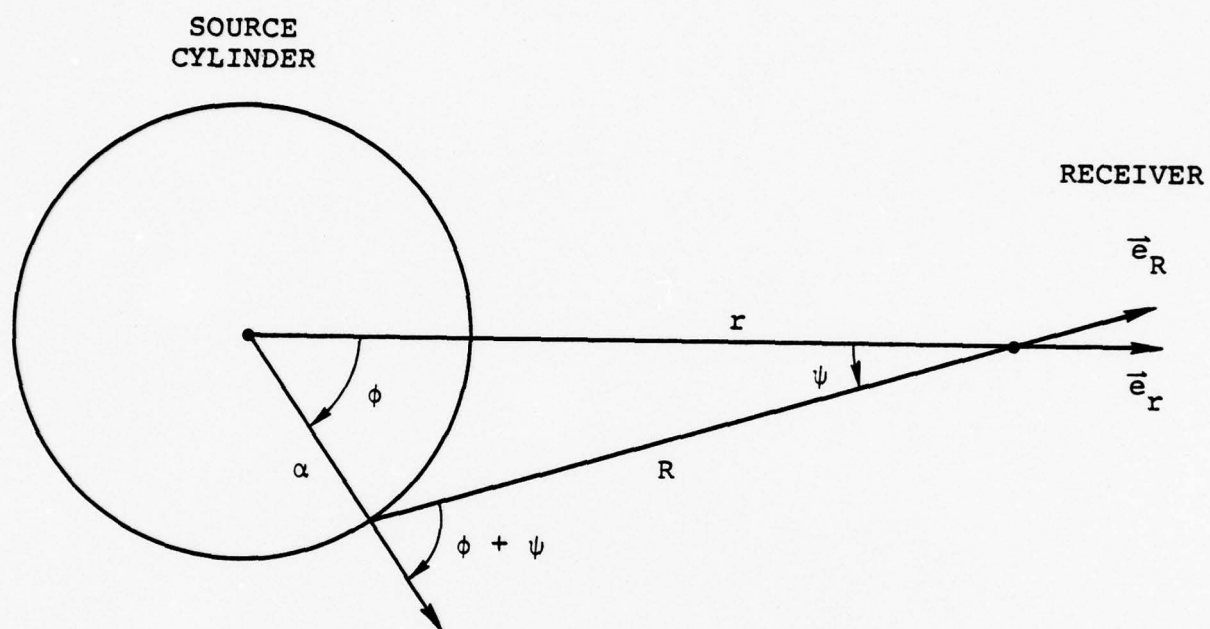


Figure 3.1. Source-receiver geometry for point forces present on the source cylinder.

The azimuthally integrated Green's tensor can be written

$$\bar{g}_{i,j} = \frac{1}{4\pi\rho\omega^2} \int_0^\infty k dk \int_0^{2\pi} d\phi [\tilde{A}_{ij}^\alpha + \tilde{A}_{ij}^\beta] \quad (3.2)$$

where

$$\tilde{A}_{ij}^\alpha = \frac{e^{-\nu_\alpha |z-z_0|}}{\nu_\alpha} \begin{bmatrix} -k^2 e^{-i\phi} \frac{dJ_1(kR)}{dkR} & \epsilon k \nu_\alpha J_1(kR) e^{i\psi} \\ \epsilon k \nu_\alpha e^{-i(\phi+\psi)} J_1(kR) & \nu_\alpha^2 J_0(kR) \end{bmatrix}$$

$$\tilde{A}_{ij}^\beta = \frac{e^{-\nu_\beta |z-z_0|}}{\nu_\beta} \begin{bmatrix} \left(\nu_\beta^2 J_0(kR) - \frac{k^2 J_1(kR)}{kR} \right) e^{-i\phi} & -\epsilon k \nu_\beta J_1(kR) e^{i\psi} \\ -\epsilon k \nu_\beta e^{-i(\phi+\psi)} J_1(kR) & -k^2 J_0(kR) \end{bmatrix}$$

with

$$R = (r^2 + a^2 - 2r a \cos\phi)^{1/2}$$

To evaluate these integrals we note the following summation theorems for Bessel functions (Gradshteyn and Ryzhik, 1965):

$$J_\nu(kR) e^{i\nu\psi} = \sum_{m=-\infty}^{\infty} J_m(ka) J_{m+\nu}(kr) e^{im\phi}$$

and

$$\frac{J_\nu(kR)}{R^\nu} = \frac{2^\nu}{k^\nu} \Gamma(\nu) \sum_{m=0}^{\infty} (v+m) \frac{J_{m+\nu}(ka)}{a^\nu} \frac{J_{m+\nu}(kr)}{r^\nu} \times C_m^\nu(\cos\phi)$$

where C_m^v is a Gegenbauer polynomial. Expanding the terms in Equation (3.2) with azimuth dependences, we have

$$\begin{aligned} \frac{dJ_1(kR)}{dkR} e^{-i\phi} &= \left(J_0(kR) - \frac{dJ_1(kR)}{dkR} \right) e^{-i\phi} = \sum_{m=-\infty}^{\infty} J_m(ka) J_m(kr) e^{i(m-1)\phi} \\ &\quad - 2 \sum_{m=0}^{\infty} (m+1) \frac{J_{m+1}(ka)}{ka} \frac{J_{m+1}(kr)}{kr} C_m^1(\cos\phi) e^{i\phi} \end{aligned}$$

$$J_1(kR) e^{i\psi} = \sum_{m=-\infty}^{\infty} J_m(ka) J_{m+1}(kr) e^{im\phi}$$

$$J_1(kR) e^{-i(\phi+\psi)} = - \sum_{m=-\infty}^{\infty} J_m(ka) J_{m-1}(kr) e^{i(m-1)\phi}$$

$$J_0(kR) = \sum_{m=-\infty}^{\infty} J_m(ka) J_m(kr) e^{im\phi}$$

In all but one of the expansions above, the ϕ dependence is now only in the argument of a complex exponential. When integrating over ϕ , all but one term in each expansion will vanish. The term involving the Gegenbauer polynomial requires special attention. Given the identity

$$C_m^1(\cos\phi) = \frac{\sin(m+1)\phi}{\sin\phi},$$

the azimuthal integration is then

$$\int_0^{2\pi} d\phi \frac{\sin(m+1)\phi}{\sin\phi} \cos\phi = 0 \quad m \text{ even}$$

$$2\pi \quad m \text{ odd}.$$

(Gradshteyn and Ryzhik, 1965). We can write

$$\int_0^{2\pi} d\phi \frac{J_1(kR)}{kR} e^{-i\phi} = \frac{8\pi}{(ka)(kr)} \sum_{m=0}^{\infty} m J_{2m}(ka) J_{2m}(kr) \quad (3.3)$$

For the surface wave solution we are interested in only far-field contributions. The integral in Equation (3.3) is bounded by $2\pi/k(r-a)$ so when $kr \gg 1$ and $r \gg a$, this term is negligible. It should be noted that even in near-field cases, evaluation of this term would present no problems, since the infinite series on the right will converge quite rapidly for small values of the arguments.

Compiling the azimuthally integrated terms we are left with the azimuthally averaged Green's functions which, neglecting the near field term, can be written

$$\bar{g}_{ij} = \frac{1}{2\rho\omega^2} \int_0^{\infty} k dk \left[\bar{A}_{ij}^{\alpha} + \bar{A}_{ij}^{\beta} \right] \quad (3.4)$$

where

$$\bar{A}_{ij}^{\alpha} = \frac{e^{-v_{\alpha}|z-z_0|}}{v_{\alpha}} \begin{bmatrix} -k^2 J_1(ka) J_1(kr) & \epsilon k v_{\alpha} J_0(ka) J_1(kr) \\ -\epsilon k v_{\alpha} J_1(ka) J_0(kr) & v_{\alpha}^2 J_0(ka) J_0(kr) \end{bmatrix}$$

$$\bar{A}_{ij}^{\beta} = \frac{e^{-v_{\beta}|z-z_0|}}{v_{\beta}} \begin{bmatrix} v_{\beta}^2 J_1(ka) J_1(kr) & -\epsilon k v_{\beta} J_0(ka) J_1(kr) \\ \epsilon k v_{\beta} J_1(ka) J_0(kr) & -k^2 J_0(ka) J_0(kr) \end{bmatrix}$$

To find the surface wave contributions due to a source described above, we must first consider the complete

multilayered problem. The contribution due to a source embedded in a multilayered elastic medium can be expressed by a homogeneous solution valid within each layer plus a source contribution inserted as a particular solution into the layer contribution containing the source. When the boundary conditions are satisfied at each layer boundary, it can be shown (Haskell, 1953) that the solution to the displacement field evaluated at the surface can be written in the form

$$U(\omega) = \int_0^{\infty} k dk \frac{F(k, \omega, z_0)}{G(k, \omega)} J_m(kr)$$

where the function $G(k, \omega)$ is independent of any source contributions. The surface wave contribution arises from singularities in the above integral occurring when the function $G(k, \omega)$ vanishes.

If we are interested only in the surface wave contribution, we need to find the k, ω pairs where the above integral is singular and compute the residues given an appropriately deformed contour in the complex k plane. Harkrider (1964) showed that the residues can be expressed in a rather convenient form. For example, the Rayleigh wave Green's tensor components for a point force embedded at depth z_0 and receiver at the surface can be written

$$g_{ij} = \frac{iA_R}{2} \begin{bmatrix} X(0) X(z_0) \frac{dH_1^{(2)}(k_n r)}{dkr} \cos\phi & -iX(0) W(z_0) H_1^{(2)}(k_n r) \\ iX(z_0) H_1^{(2)}(k_n r) \cos\phi & -W(z_0) H_0^{(2)}(k_n r) \end{bmatrix} \quad (3.5)$$

where

- $k_n(\omega)$ = horizontal wave number associated with the n-th Rayleigh mode for a frequency ω
 $A_R(k_n)$ = medium amplitude response function
 $X(k_n, z)$ = real normalized horizontal displacement eigenfunction
 $W(k_n, z)$ = normalized vertical displacement eigenfunction
 $H_m^{(2)}(k_n r)$ = Hankel function of the second kind of order m.

For a given set of frequencies, the programs of Harkrider (1970) can be used to compute all of the above parameters for a given Rayleigh wave mode. Equation (3.5) is the surface wave equivalent of Equation (3.1).

Since we know that the source contribution enters into the complete solution in a multilayered medium as particular solution only, we can write down the surface wave solution for an azimuthally integrated axisymmetric source immediately (surface wave equivalent of Equation (3.4)).

$$\bar{g}_{ij} = \pi i A_R \begin{bmatrix} X(0) X(z_0) J_1(ka) H_1^{(2)}(kr) & -iX(0) W(z_0) J_0(ka) H_1^{(2)}(kr) \\ -iX(z_0) J_1(ka) H_0^{(2)}(kr) & -W(z_0) J_0(ka) H_0^{(2)}(kr) \end{bmatrix} \quad (3.6)$$

If we make the far-field approximation $kr \gg 1$, we can employ an asymptotic representation of the Hankel functions

$$H_m^{(2)}(kr) = \sqrt{\frac{2}{\pi kr}} e^{-i(kr - \frac{\pi m}{2} - \frac{\pi}{4})}$$

The resulting far-field surface wave Green's tensor components are

$$\bar{g}_{ij} \approx i \sqrt{\frac{2\pi}{kr}} A_R e^{-ikr - \frac{i\pi}{4}} \begin{bmatrix} -X(0)X(z_0)J_1(ka) & iX(0)W(z_0)J_0(ka) \\ X(z_0)J_1(ka) & -iW(z_0)J_0(ka) \end{bmatrix} \quad (3.7)$$

Note that the horizontal and vertical spectral displacements differ only by a factor $-X(0)$, the surface ellipticity for Rayleigh waves. Without loss of generality, we can continue by examining only the vertical component of displacement.

To obtain the analytical continuation of motion from a cylindrical source region, we will need the derivatives of the Green's tensor with respect to z_0 and the source radial variable, which we will now call r_0 :

$$\frac{\partial g_{zr}}{\partial r_0} = ik \sqrt{\frac{2\pi}{kr}} A_R e^{-ikr - \frac{i\pi}{4}} X(z_0) \frac{dJ_1(kr_0)}{dkr_0}$$

$$\frac{\partial g_{zz}}{\partial r_0} = - \sqrt{\frac{2\pi}{kr}} A_R e^{-ikr - \frac{i\pi}{4}} W(z_0) J_1(kr_0)$$

and using identities in Harkrider (1970)

$$\frac{\partial g_{zr}}{\partial z_0} = ik \sqrt{\frac{2\pi}{kr}} A_R e^{-ikr - \frac{i\pi}{4}} J_1(kr_0) \left[W(z_0) + \frac{\tau(z_0)}{u} \right]$$

$$\frac{\partial g_{zz}}{\partial z_0} = -k \sqrt{\frac{2\pi}{kr}} A_R e^{-ikr - \frac{i\pi}{4}} J_0(kr_0) \left[\frac{X(z_0) + \Sigma(z_0)}{(1 + 2\nu)} \right]$$

where $\tau(z_0)$ and $\Sigma(z_0)$ are the normalized horizontal and vertical stress eigenfunctions, respectively.

Finally, if we are given monitored stresses and displacements on a cylinder of radius a and depth b enclosing the source region, we can use the expressions in Rodi, et al.

(1978) to calculate the displacement field in the elastic medium. Since we are dealing with Fourier transformed Green's functions and monitored quantities here, all time convolutions become products in the formulas. Substituting into Equation (3.2) of Rodi, et al. (1978) we have

$$\begin{aligned}
 U_z(r, 0, \omega) = & a \int_0^b dz_0 \left[-iX(z_0) J_1(ka) \bar{\sigma}_{rr}(a, z_0) \right. \\
 & - W(z_0) J_0(ka) \bar{\sigma}_{rz}(a, z_0) + \left. \left[(\lambda + 2\mu) ikX(z_0) \frac{dJ_1(kr_0)}{dkr_0} \right]_{r_0=a} \right. \\
 & + i\lambda \frac{X(z_0)}{a} J_1(ka) - \frac{\lambda k J_0(ka)}{(\lambda + 2\mu)} \left[\lambda X(z_0) + \Sigma(z_0) \right] \bar{U}_r(a, z_0) \\
 & + \left[-\mu kW(z_0) J_1(ka) + i\mu k J_1(ka) \left[W(z_0) \right. \right. \\
 & + \left. \left. \frac{\tau(z_0)}{\mu} \right] \right] \bar{U}_z(a, z_0) \left. + \int_0^a r_0 dr_0 \left[-iX(b) J_1(kr_0) \bar{\sigma}_{rz}(r_0, b) \right. \right. \\
 & - W(b) J_0(kr_0) \bar{\sigma}_{zz}(r_0, b) + \left[i\lambda kX(b) \frac{dJ_1(kr_0)}{dkr_0} \right. \\
 & - k[\lambda X(b) + \Sigma(b)] J_0(kr_0) + \left. \left. \frac{\lambda}{r_0} \right] \bar{U}_z(r_0, b) \right. \\
 & + \left[-\mu kW(b) J_1(kr_0) + i\mu k \left[W(b) \right. \right. \\
 & + \left. \left. \frac{\tau(b)}{\mu} \right] J_1(kr_0) \right] \bar{U}_r(r_0, b) \left. \right] \quad (3.8)
 \end{aligned}$$

The horizontal spectral displacement $U_r(r, 0, \omega)$ is simply $-X(0) U_z(r, 0, \omega)$.

3.3 IMPLEMENTATION

The formulation above is being programmed and tested. Evaluation of Equation (3.8) is straightforward and should present few difficulties. Except for the monitored displacements and stresses, all information needed is standard output of the programs of Harkrider (1970). For many problems of interest, Equation (3.8) could be simplified a great deal. For long period surface waves, where wave lengths are much larger than the dimensions of the source region, the surface wave eigenfunctions needed would essentially be constants. The stress eigenfunctions $\Sigma(z_0)$ and $\tau(z_0)$ could be made zero, $W(z_0)$ unity, and $X(z_0)$ the surface ellipticity. The source contribution from the depth integral would be simply an average of the monitored values with depth. The radial integral could be simplified using the $J_0(kr_0) \approx 1$ and $J_1(kr_0) \approx kr_0/2$ for $(kr_0)^2 \ll 1$. Under these assumptions and including only the lowest order terms, the vertical displacement spectrum could be approximated by

$$U(r, 0, 0) = \sqrt{\frac{2\pi}{kr}} A_R e^{-ikr - \frac{i\pi}{4}} \times \int_0^a \left(\lambda \bar{U}_z(r_0, b) - r_0 \bar{\sigma}_{zz}(r_0, b) \right) dr_0 \\ + a \int_0^b \left[kX(0) \left[i(\lambda + 2\mu) - \frac{\lambda^2}{(\lambda + 2\mu)} \right] \bar{U}_r - \bar{\sigma}_{rz} \right] dz$$

The algorithm given here requires the spectra of displacements and stresses computed by numerical methods. Problems occasionally may arise because often the periods of surface wave motion of interest may be much longer than the duration of the computed source displacements. In such cases

spectral values at the periods of interest will have to be interpolated from discrete values computed numerically. The accuracy of interpolation of the long periods may be rather sensitive to whether or not static values are reached in the source simulations. Such problems will probably have to be dealt with on a case-by-case basis.

IV. SOURCE CALCULATIONS

We have initiated an extensive review of our one-dimensional spherically symmetric calculations of the ground motion and source functions due to nuclear explosions in salt (the SALMON event), in NTS granite (PILEDRIVER) and Rainier Mesa tunnel tuff. The primary purpose of this review is to update and improve our nonlinear constitutive models while insuring that they are compatible with our two-dimensional codes. With the updated models, we plan to investigate such two-dimensional effects as nonhydrostatic in situ stress conditions, depth of burial and spall and slapdown at the free surface.

The most important modeling changes to date are the implementation of good equations-of-state for the cavity gases to replace the constant γ ideal gas treatment, improvements which make the overburden pressure treatment consistent with our equations of state, and the development of a better effective stress law to model the influence of water saturation in rocks. Here we present discussion of our latest one-dimensional calculations for PILED RIVER, SALMON, and Rainier Mesa (Area 12) saturated tuff, and discuss the modeling improvements made for each. Table 4.1 gives the material properties used for the source function calculations. A complete discussion of the basic constitutive modeling may be found in Bache et al. (1975) or Cherry, Rimer, and Wray (1975).

PILED RIVER

It is well known that the measured velocity profiles for PILED RIVER, a 61 kt event in NTS fractured granodiorite (Perret, 1968), cannot be matched using the triaxial failure envelope measured in the laboratory. A reasonable approximation to the laboratory failure envelope is a parabola of the form

$$Y = Y_0 + Y_m \frac{\bar{P}}{\bar{P}_m} \left(2 - \frac{\bar{P}}{\bar{P}_m} \right)$$

TABLE 4.1

MATERIAL PROPERTIES USED FOR SOURCE FUNCTION CALCULATIONS

MATERIAL PROPERTIES USED FOR SOURCE FUNCTION CALCULATIONS															At 20 Ton Yield				
NAME	gm/cm ³	α	km/sec	μ	kbars	Y _m	kbars	Y _O	kbars	P _m	%	kbars	P _e	kbars	P _O	3			R _e
																m ³	ψ _∞	R _C	
PILED DRIVER																			
310 ¹	2.67	5.33	207		7.7	0.3	9.0	0	1.0	0		120	9.23	3.13	50.1				
410	2.65	5.345	207		7.7	0.3	9.0	0.1 ₂	2.0	0.2		120	3.77	2.51	48.7				
407	2.65								1.0				5.77	2.90	46.8				
411									0.5				6.42	3.06	43.9				
SALMON																			
252	2.15	4.2	125		0.467	0.066	0.42	0	0	0		175	4.1	~2.9	~26.0				
408	2.162	4.27	125		0.467	0.033	1.25	0	0	0		175	7.8	3.48	43.5				
414					0.64	0.04	0.54					175	4.8	2.95	27.7				
415					0.64	0.04	0.54					55	5.3	3.02	60.5				
Area 12 Tuff																			
127 ¹	1.91	2.4	40		0.35	0.05	2.0	1.6	0.5	0.02		56	14.5	6.12	~40.0				
409	1.91	2.4	32.4		0.33	0.07	2.0	1.6	2.0	0.1		75	9.8	3.875	32.3				
412	same as 409	with new effective stress law																	
416	same as 412	with smaller source (20.7 tons/kt)																	
413	same as 416	except with still smaller source (8.75 tons/kt)																	

1. Old relaxation effective stress law, cavity treatment, and overburden treatment
2. Voids used for effective stress law only.

where Y is the maximum stress difference, Y_o , Y_m , and \bar{P}_m are constants of the fit (given in Table 4.1), and

$$\bar{P} = P - \frac{1}{2} \left(\frac{J'_3}{2} \right)^{1/3}$$

where J'_3 is the third deviatoric stress invariant.

Calculation 310 of Table 4.1 and calculation 130 of Bache et al. (1975) were successful attempts to reproduce the free field velocity data of Perret (1968) through the concept of an "effective stress law." In the highly nonlinear near field regime this allowed us to use a much lower failure envelope while retaining the laboratory failure surface outside the range where the maximum stress is less than P_c . The effective stress concept may be simply stated. For pressure dependent failure envelopes the effective pressure, $P - P_w$, where P_w is the pore water pressure, should be used to determine Y rather than the mean stress. For rocks containing air-filled porosity ϕ , the maximum stress level P_c can reasonably be chosen as the crush pressure, the pressure at which all air-filled porosity is irreversibly removed, since the pore water can hardly be expected to carry much of the load while voids remain open. For PILEDRIVER, water is assumed present in the existing fractures, rather than in the negligible porosity.

The simple effective stress model (we shall call this the relaxation model) used in calculation 310 and in the DNA study (Bache et al. (1975)) assumed that if the mean stress in an element ever exceeded P_c , that material would forever have a zero effective stress, implying a much lower failure surface. The stress deviator would be allowed to relax down to the low failure surface in some relaxation time, δ . If the mean stress never exceeded P_c , the laboratory failure surface would be used. This relaxation scheme was used for the DNA study for NTS granite, Pahute Mesa tuffs and rhyolites, Rainier Mesa saturated tuff, and Yucca Flat saturated and relatively dry tuff and was found to

give a consistent set of equivalent elastic sources which could explain most of the teleseismic data from NTS events. However, the relaxation model has several drawbacks; (1) the results depend on an arbitrary parameter δ , the relaxation time which scales with yield. (2) The discontinuous change in models at the range of maximum pressure P_c results in enhanced tensile fracturing in some cases. (3) For materials with negligible air-filled voids, such as granite or rhyolite, P_c itself is chosen somewhat arbitrarily. We avoided some of these difficulties by calibrating δ and P_c to the PILEDRIVER near field data and using the same δ for all calculations of the study (if the material had no voids, the same P_c was also used throughout).

We have now developed an effective stress law which, for a material having negligible air-filled voids, has no free parameters. We relate the change in air-filled porosity directly to the effective stress and assume that below some elastic pressure, P_e , the effective stress is the mean stress. As the voids are crushed, the effective stress reduces to zero smoothly at the crush pressure. For PILEDRIVER, a material with negligible air-filled porosity, we assumed that a small amount of voids were present and created a crush curve. However, this crush curve was not used in computing the material pressure but was used only for the effective stress computations to give a smooth transition between regions. The results do not depend much on P_e but are quite dependent on P_c . We again calibrated our model using the PILEDRIVER near field velocity data and cavity radius data.

For calculation 410 of Table 4.1 with $P_c = 2$ kbars, the computed cavity radius (based on a yield of 20 tons) was far too small. However, both calculations 407 and 411 gave reasonable cavity radii and near field velocity profiles (the measured cavity radius scales to 3.07 meters at 20 tons). Figures 4.1 and 4.2 show the calculated velocity profiles compared to

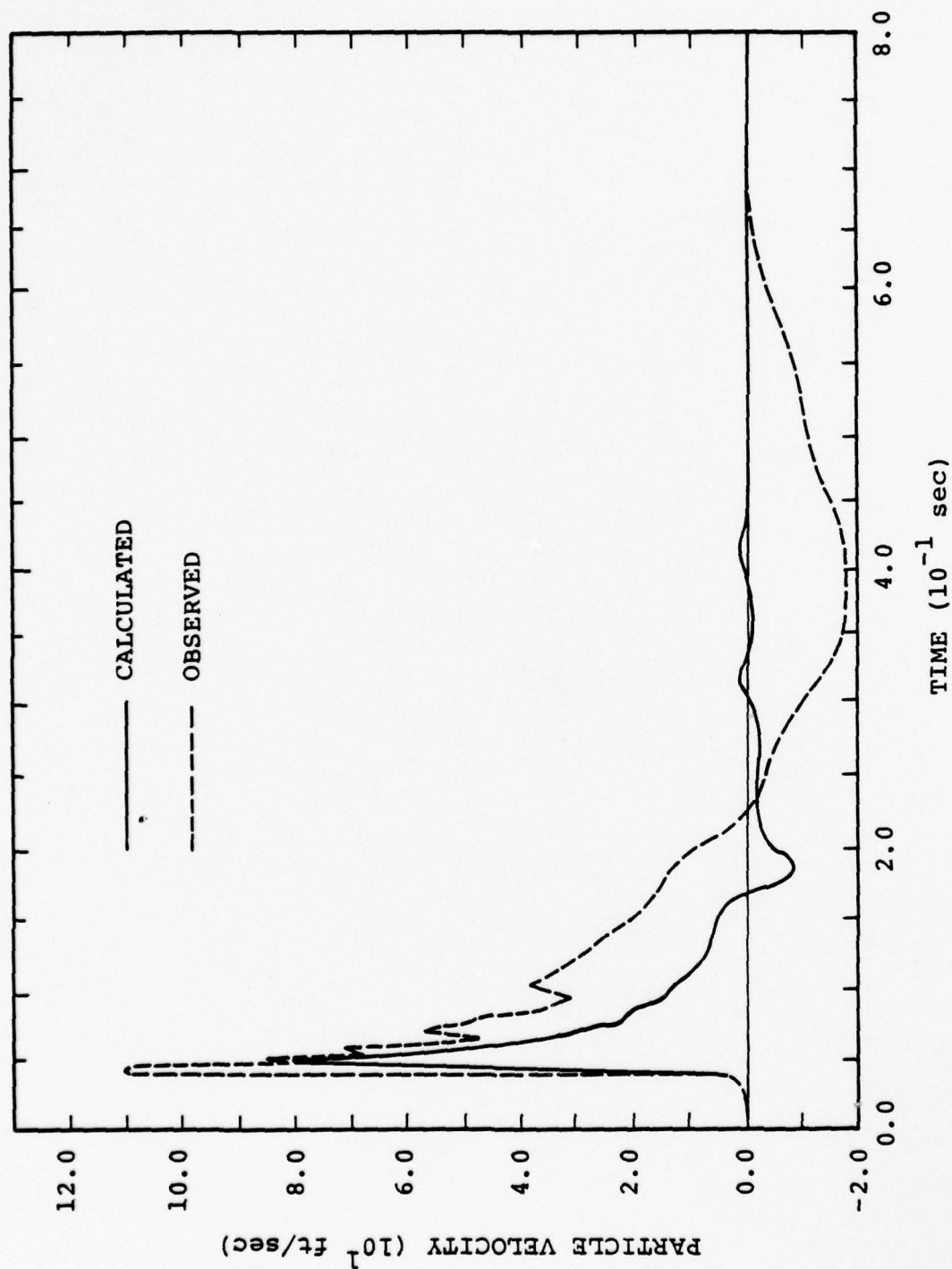


Figure 4.1. Particle velocity versus time at a range of 668 feet for PILEDRIVER (61 kt) calculation 411.

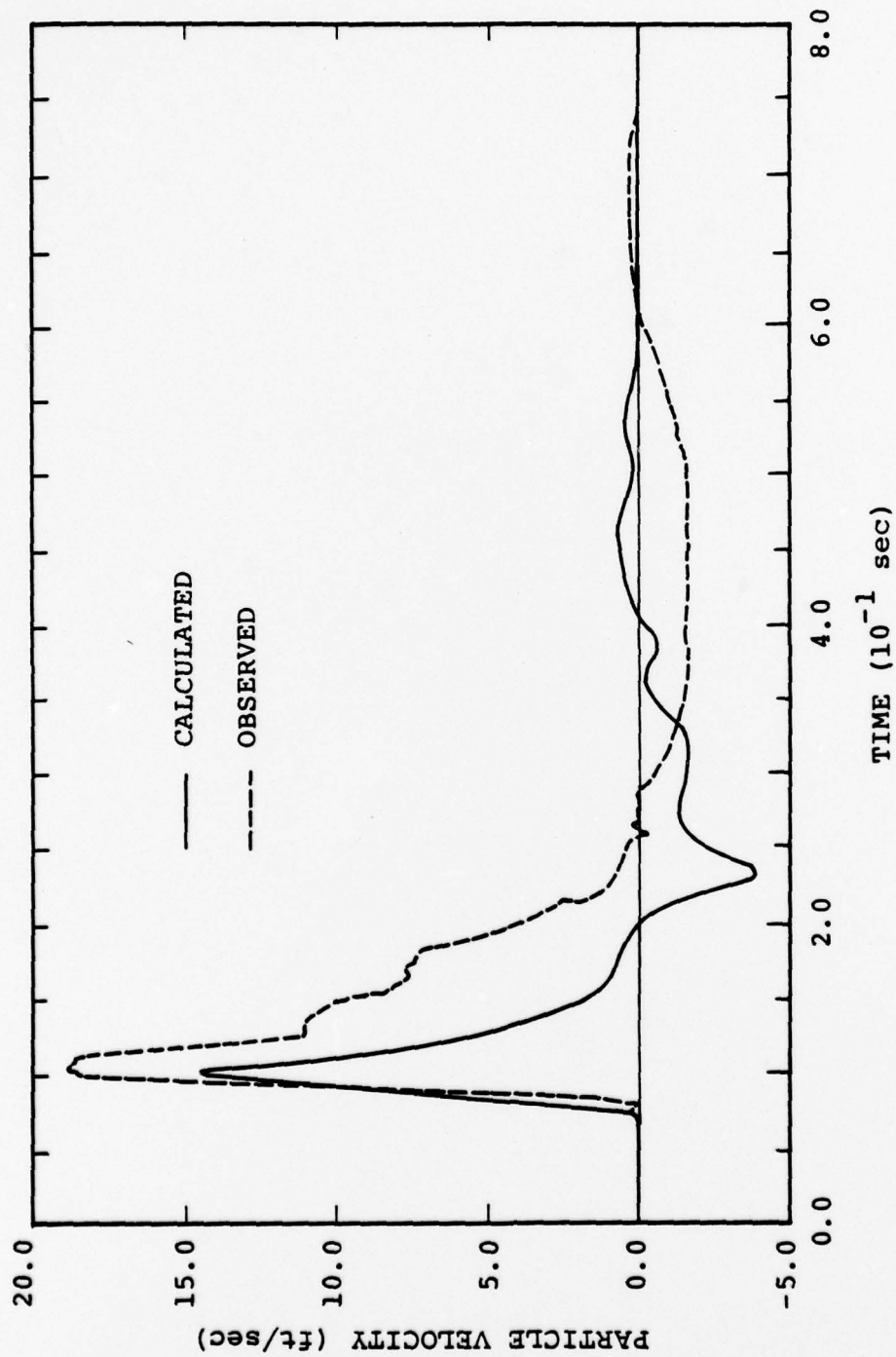


Figure 4.2. Particle velocity versus time at a range of 1543 feet for PILEDRIVER (61 kt) calculation 411.

the measured velocity at two recording stations (Perret, 1968). Peak velocities are in good agreement with the data. However, overall the waveforms are not in as good agreement with the observations as were the computed waveforms given by Bache, et al., (1975). Figure 4.3 shows the computed reduced velocity potential transforms for calculations 410, 407 and 411 together with the results for 310. The study shows that the higher the crush pressure, the lower the RDP and the more peaked the spectrum. These relationships are reasonable since a higher P_c implies a higher strength, therefore a smaller cavity and smaller ψ_∞ . The peaking of the spectrum is a function of the amount of tensile cracking, since a higher strength implies more cracking, since a higher strength implies more cracking, the results are consistent with intuition. Either 407 or 411 is acceptable based on near field data, cavity size, peak velocity, stress, etc.

There are two other major modeling differences between 310 and the more recent calculations. The newer calculations have considerably better treatment of the hydrostatic overburden and of the cavity gases. In the older calculations, the scalar overburden pressure was simply added to the pressure obtained from the granite equation of state. For the newer calculations, the ambient rock was compressed initially in the code in order to recover the overburden pressure directly from the equation of state. This procedure is more consistent and will allow us to input simply a depth dependent prestress for the two-dimensional calculations.

Finally, the newer calculations have a far better equation of state for the cavity. Until recently we placed the device energy in a rock sphere having a mass of 70 metric tons per kiloton of device yield and calculated the pressure using an ideal gas equation of state with a constant γ of 1.4. We are now using the quartz (SiO_2) equation of state to describe the cavity gases. This equation of state, developed by Pyatt and Baker (1978), models the rock behavior from gas pressures of many megabars down to pressures of several bars including the known phase changes. At present we are still placing the

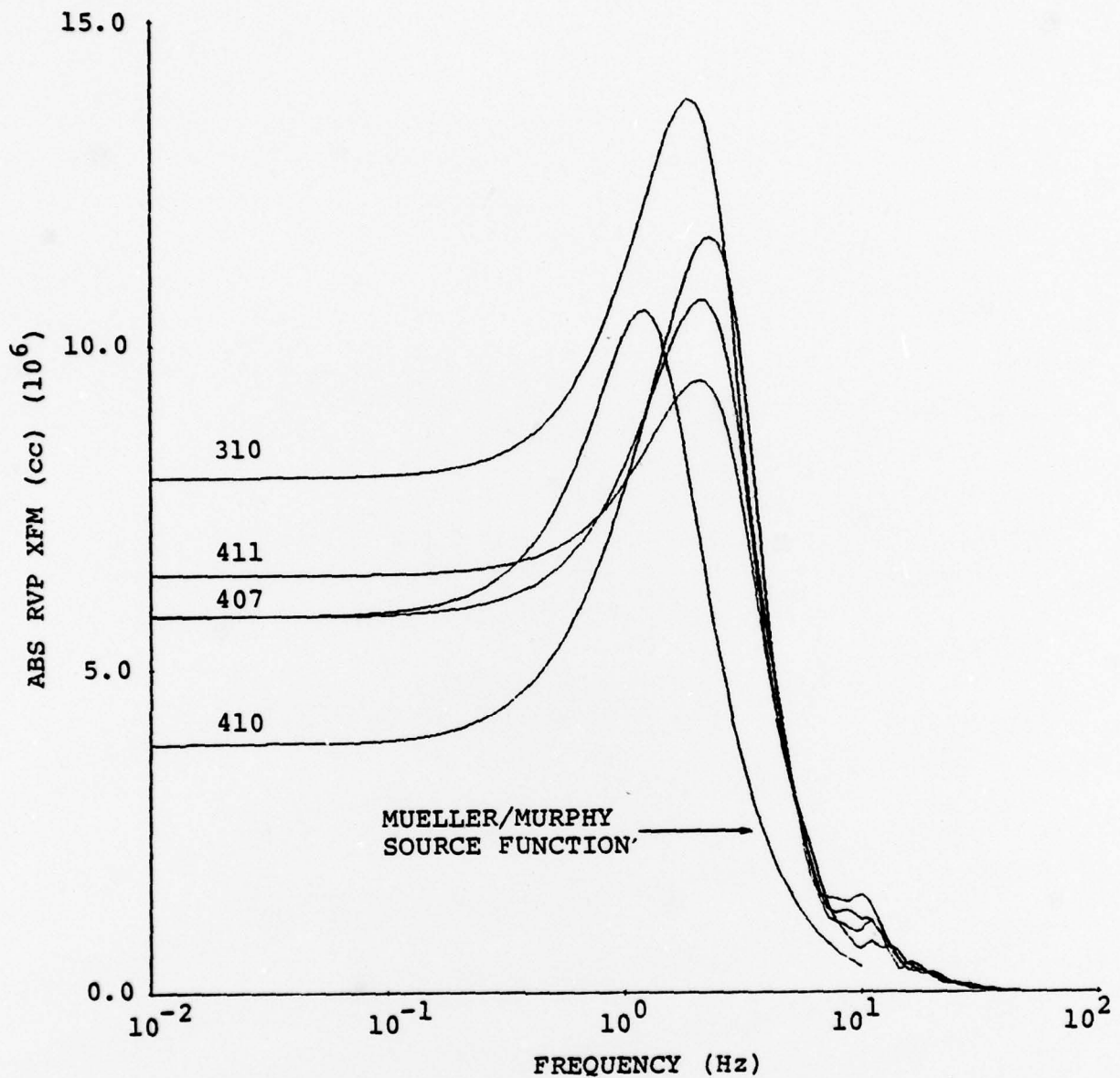


Figure 4.3. Equivalent source functions for PILEDRIVER calculations. The frequency axis is scaled to 61 kt, the amplitude axis to 0.02 kt. Calculations 410, 407 and 411 show the effect of decreasing P_c . Also shown is the Mueller/Murphy source function scaled to the PILEDRIVER yield and depth.

device energy in a 70 ton per kiloton rock sphere. Tests are now underway which examine the importance of a smaller initial source.

Also shown in Figure 4.3 is the Mueller/Murphy source function (Mueller and Murphy, 1971) scaled to the PILEDRIVER yield and depth. This source function is based on a fit to the SHOAL data and gives a reasonable approximation to the PILEDRIVER data (Murphy, 1977), though it should be kept in mind that the measured source functions for PILEDRIVER vary over an order of magnitude. The main difference between the Mueller/Murphy source function and those computed is that the later peak at higher frequencies.

SALMON

SALMON was a 5.3 kt nuclear event detonated in the Tatum salt dome in southern Mississippi in 1964. We describe here our most recent calculations of the SALMON event and indicate the direction of our present efforts. Numerous unsuccessful attempts have been made to calculate the SALMON reduced displacement potential (RDP). The basic difficulty is that the calculated RDP for a salt failure envelope as measured by triaxial loading in the laboratory (Pratt, 1978; Heard, et al., 1975) is significantly smaller than the measured RDP (see Murphy 1977). If a lower failure envelope is used to raise the calculated RDP, the calculated cavity radius becomes too large when compared with drillback measurements in the SALMON cavity.

Figure 4.4 shows the calculated source spectra for the material properties data shown in Table 4.1. Calculation 252 uses constant γ ideal gas treatment for the cavity and has been reported previously by Bache, Cherry and Mason (1976). The rest of the calculations used cavity equation of state for salt derived using the EIONX equation of state (Pyatt (1966)). EIONX is a simple mathematic model which incorporates

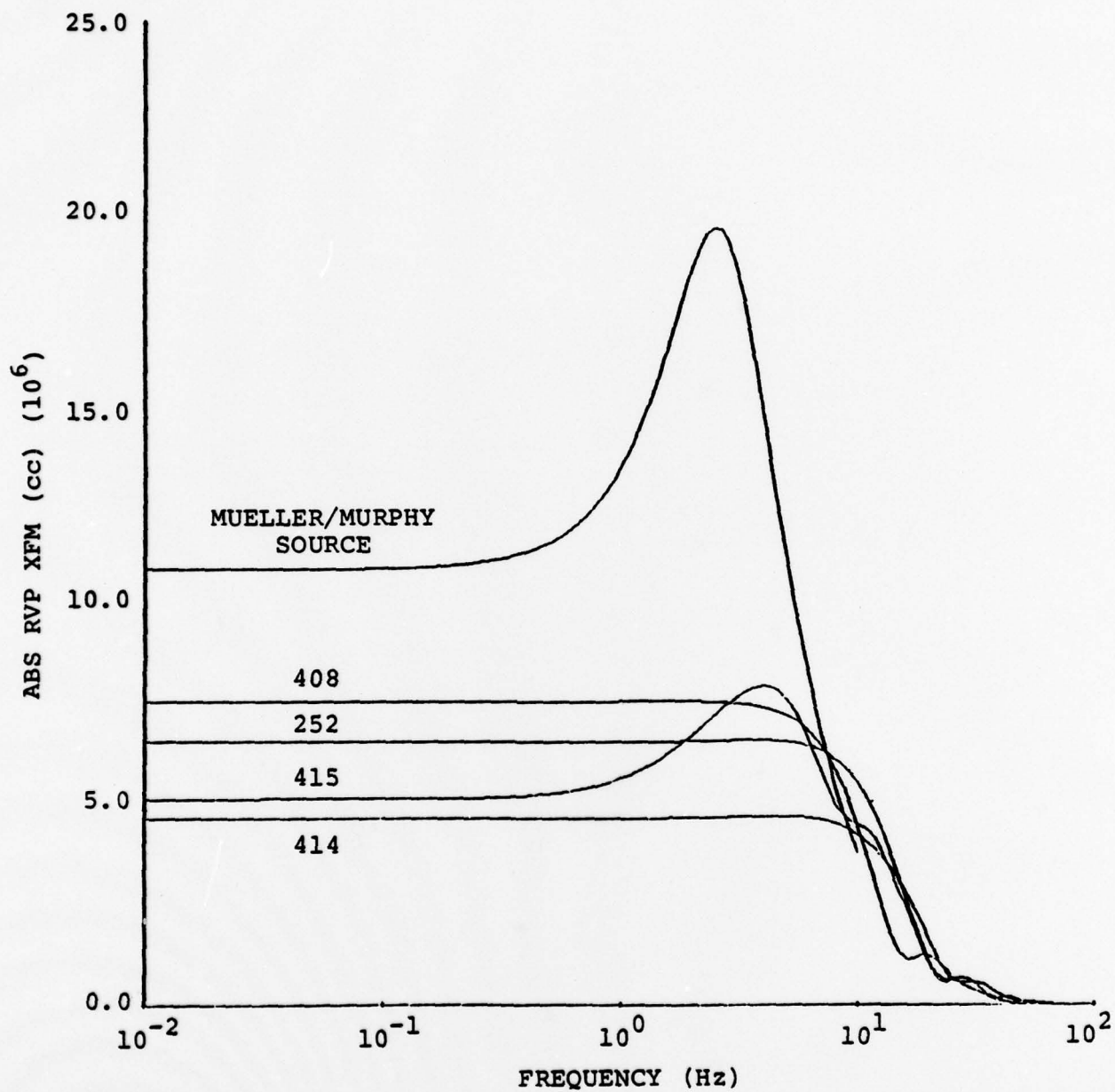


Figure 4.4. Equivalent source functions for SALMON calculations. The frequency axis is scaled to 5.3 kt, the amplitude axis to 0.02 kt.

many of the important features of the more complicated Saha equation models. The new overburden pressure treatment was also used for these calculations. No effective stress law was used for the dry salt dome.

Also shown in Figure 4.4 is the Mueller/Murphy source function for SALMON (Mueller and Murphy, 1971). Since this source function is based on a fit to the SALMON near field observations, it is shown as a convenient representation for the observed data.

Calculation 408 used the lowest possible failure surface which we could justify (based on the uniaxial measurements of Heard, et al. (1975)). The calculated RDP of 7.8 m^3 for 20 ton yield (see Table 4.1) was still considerably lower than the measured value (approximately 11 m^3 for 20 tons). Yet the calculated cavity radius was significantly higher than 2.8 m, the measured value scaled to 20 tons yield. Calculation 414 represents our best guess for a failure envelope, based on the available triaxial data, in particular the data from Terra Tek, Incorporated (Pratt, 1978) and gives a reasonable cavity radius, peak stresses and velocities. However, the calculated RDP was more than a factor of two low.

We plan next to investigate whether a two-dimensional in situ stress field (in uniaxial strain) can influence the RDP. At shot depth there is a vertical stress of approximately 175 bars and a horizontal stress of 55 bars. Calculation 415 (made with a scalar overburden pressure of 55 bars) gave a slightly higher ψ_∞ and cavity radius than calculation 414. However, unlike the rest of the calculations, the spectra was quite peaked due to a large amount of tensile cracking. Due to this cracking, the elastic radius R_e was more than twice as large as for calculation 414.

If in situ stress proves not to be the explanation of our low calculated RDP, then it is likely that our constitutive

models for salt are inadequate. In that event, we plan to include viscoelastic effects in constitutive model, possibly through a Maxwell solid approach.

Area 12 Tuff

The saturated tuffs of Rainier Mesa are unique at NTS in that they have been characterized by an enormous number of laboratory measurements of material properties data. Although the variation in material properties from event to event is considerable, we have been able in the last few years to compile a series of "average" Area 12 tunnel tuff material properties data which tend to be valid for the more recent nuclear events. A series of SKIPPER calculations have recently been completed for these average tuff properties (Table 4.1, calculation 409) which look at the effects of initial cavity size and of the new effective stress law on source spectra.

We were able to investigate the effect of initial cavity size through the use of the CHEST 24 tuff chemical equilibrium equation of state which was developed by Laird (1976), and which accurately models the rock behavior in pressure regimes from tens of megabars down to a few tenths of a bar. This tabular equation of state has been created especially for use with hydrodynamic codes to study nuclear explosion phenomenology. It couples an elaborate chemical equilibrium treatment with steam tables and bulk modulus data. The CHEST equation of state was used to describe the tuff both inside and outside of the cavity.

Figure 4.5 shows source spectra for the tuff calculations listed in Table 4.1. Calculation 127 from the Bache, et al., (1975) study used a smaller overburden pressure causing the spectra peak to be at a lower frequency. This calculation, using the old "relaxation" effective stress law, gave a cavity radius of 6.12 meters at the 20 ton yield. This is far greater than the 3.72 to 4.41 meter range for the measured cavity radii.

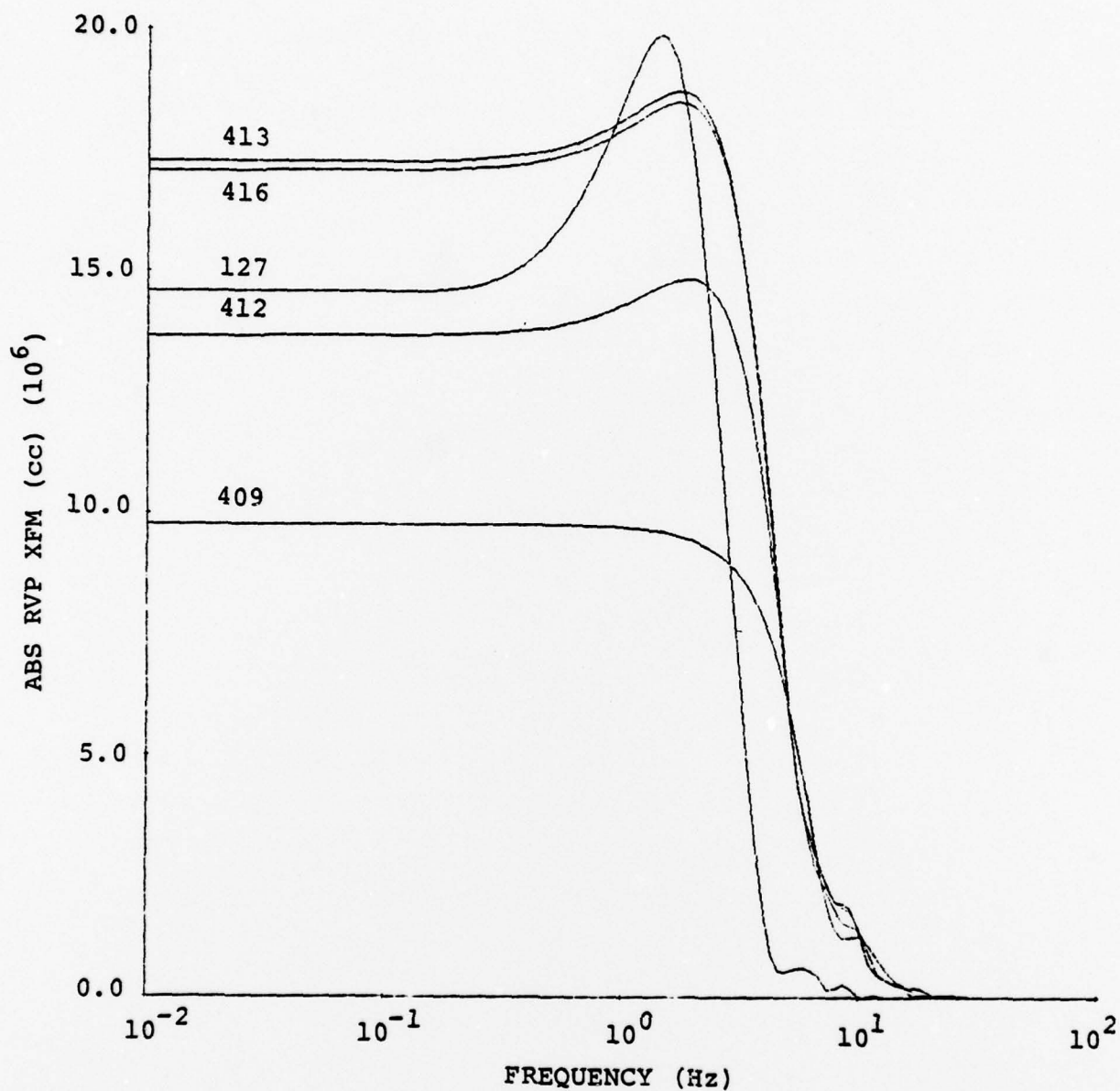


Figure 4.5. Equivalent source functions for Area 12 tuff. The frequency axis is scaled to 10 kt, the amplitude axis to 0.02 kt. All calculations but 127 (from Bache, et al., 1975) have identical material properties. Calculation 409 (no effective stress law) and 412 (with new effective stress law) have 70 ton/kt initial cavities. Calculations 412, 416 and 413 respectively show the effect of smaller initial cavity size.

Calculation 412 used CHEST 24, the new effective stress law, and the new overburden pressure treatment. It gave a cavity radius of 4.30 meters, well within the data range. Calculation 409 had no effective stress law, but otherwise had the same modeling and data as 412. The calculated cavity radius of 3.875 meters was well within the band of measured data.

A comparison of the three calculations indicates that the old effective stress law results in more peaked spectra than is seen for the newer effective stress law. For no effective stress law (Calculation 409), the spectra is not peaked at all. Calculation 412 with the new effective stress law is in better agreement with free field data.

Calculations 412, 416 and 413 have identical modeling, except for the size of the initial source. For 412, the device yield was placed in an initial cavity with radius equivalent to 70 metric tons/kt of yield, for 416 in 20.7 tons/kt, and for 413 in 8.75 tons/kt. The results for calculations 416 and 413 differ only slightly. They both show a cavity radius slightly larger than the measured values and gave approximately 25 percent greater cavity volume, ψ_{∞} , peak spectra, and volume inside the elastic radius than did calculation 412. A careful analysis was made of these rather surprising results. It was noted that the calculated melt for the 70 ton/kt initial cavity extended no further than the initial Lagrangian boundary of the cavity. For the smaller initial cavities, the melt radius (which we call the final cavity radius) extended considerably further. The analysis indicated that, for the 70 ton/kt initial cavity (412), the energy density input into the cavity cells was just sufficient to vaporize these cells. For the 20.7 ton/kt cavity (416), far more energy was input into the smaller cavity than needed to vaporize the mass present. However, the extra energy did not vaporize further cells. Since the energy required to vaporize the rock is wasted energy that could otherwise go

into driving the shock wave, the smaller initial cavity drives a stronger shock wave and therefore gives a larger final cavity and RDP. The very small initial cavity (8.75 tons/kt, calculation 413) has a sufficiently high energy density to vaporize rock out almost to the same radius as for calculation 416. Thus the results are quite similar.

The question that arises is which calculational procedure is correct? Clearly, hydrodynamic codes do not take into account some basic physical processes such as thermal conductivity or flow of vaporized water through the rock mass. Thus it becomes difficult to compute both the correct vaporization radius and the melt radius using these codes alone (equilibrium procedures have been developed which take the late-time code output and determine the true melt by mixing the reserve energy of the cavity with rock mass outside). Further study is needed in order to resolve this problem. Meanwhile we will continue to use the 70 ton/kt rock gas model for all calculations. (For the above calculations, this means using 412 which is in better agreement with the measured cavity radius data). Any small underestimate of the source spectra which may be inherent in this procedure is likely to occur in source calculations in all materials.

Summary

We have added the following features to our nonlinear constitutive models:

1. A new effective stress law which scales with device yield.
2. An improved treatment of overburden pressure which is consistent with our equations of state.
3. Better cavity equations of state for granite, salt and tuff.

Source calculations have been made with these improved models for NTS granite (PILED RIVER), salt (SALMON) and for average NTS Area 12 tunnel tuff material properties. These calculations lead to the following conclusions.

1. We are unable to calculate the SALMON RDP in one-dimension with our present models using laboratory data for the failure envelope. The calculations give the measured cavity radius but too small an RDP.
2. We can calculate the PILED RIVER RDP with these models and obtain reasonable agreement with near field velocity data and with the measured cavity radius.
3. Using the new effective stress law, we can calculate an RDP for average NTS Area 12 tuff material properties without any free parameters and obtain good agreement with measured cavity radius. We were unable to obtain good agreement with cavity radius data in our earlier studies.

Future work will be directed toward the following areas:

1. SALMON: We will attempt to calculate this event in two-dimensions to study the influence of in situ stress on the RDP. We may also introduce viscoelasticity into our constitutive models.
2. PILEDRIVER: We do not plan any further one-dimensional calculations to calibrate our models further to obtain better agreement with the Perret velocity histories. Our efforts will be directed toward two-dimensional calculations to examine the effect of depth of burial and spall on the far-field signals.
3. Cavity Modeling: The calculations for tuff have raised the question of how best to initialize our calculations. We will examine this question further.

REFERENCES

- Apsel, R. J., J. E. Luco and J. A. Orcutt (1977), "Body Wave and Surface Wave Propagation in a Multi-Layered Half-Space," abstracts with programs, Geol. Soc. Am., 9, 381.
- Bache, T. C., J. T. Cherry and B. F. Mason (1976), "The Dependence of Body Wave Magnitude on Yield for Underground Explosions in Salt," Systems, Science and Software Topical Report SSS-R-77-3057, November.
- Bache, T. C., T. G. Barker, N. Rimer, T. R. Blake, D. G. Lambert, J. T. Cherry and J. M. Savino (1975), "An Explanation of the Relative Amplitudes of the Teleseismic Body Waves Generated by Explosions in Different Test Areas at NTS," Systems, Science and Software Final Report SSS-R-76-2746 (DNA 39585).
- Burridge, R. and L. Knopoff (1964), "Body Force Equivalent for Seismic Dislocation," Bull. Seism. Soc. Am., 54, 1875-1888.
- Cherry, J. T., N. Rimer and W. O. Wray (1975), "Seismic Coupling from a Nuclear Explosion; The Dependence of the Reduced Displacement Potential on the Nonlinear Behavior of the Near Source Rock Environment," Systems, Science and Software Report SSS-R-76-2742 (submitted to ARPA), September 1975.
- Gradshteyn, I. S. and I. M. Ryzhik (1965), Tables of Integrals, Series, and Products, Academic Press, New York.
- Harkrider, D. G. (1964), "Surface Waves in Multi-Layered Elastic Media I. Rayleigh and Love Waves from Buried Sources in a Multi-Layered Elastic Half-Space," Bull. Seism. Soc. Am., 54, 627-679.
- Harkrider, D. G. (1970), "Surface Waves in Multi-Layered Elastic Media. Part II. Higher Mode Spectra and Spectral Ratios from Point Sources in Plane Layered Earth Models," Bull. Seism. Soc. Am., 60, 1937-1987.
- Haskell, N. A. (1953), "The Dispersion of Surface Waves on Multilayered Media," Bull. Seism. Soc. Am., 43, 17-34.
- Heard, H. C., A. E. Abey, B. P. Bonner and A. Duba (1975), "Stress-Strain Behavior of Polycrystalline NaCl to 3.2 GPa," Lawrence Livermore Laboratory Report UCRL-51743.

REFERENCES (continued)

- Herrmann, R. B. (1978), "A Note on Causality Problems in the Numerical Solution of Elastic Wave Propagation in Cylindrical Coordinate Systems," Bull. Seism. Soc. Am., 68, 117-124.
- Laird, D. H. (1976), "A Chemical Equilibrium Equation of State for Saturated Tuff," Systems, Science and Software Topical Report SSS-R-75-2740.
- Mueller, R. A. and J. R. Murphy (1971), "Seismic Characteristics of Underground Nuclear Detonations," BSSA, 61, 1975.
- Murphy, J. R. (1977), "Seismic Coupling and Magnitude/Yield Relations for Underground Nuclear Detonations in Salt, Granite, Tuff/Rhyolite and Shale Emplacement Media," Computer Sciences Corporation Technical Report (Draft) CSC-TR-77-0004, December.
- Murphy, J. R. (1978), "A Review of Available Free-Field Seismic Data from Underground Nuclear Explosions in Salt and Granite," Computer Sciences Corporation Report CSC-TR-78-0003.
- Perret, W. R. (1968), "Shot Piledriver: Free-Field Ground Motion in Granite," POR 4001.
- Pratt, H. R. (1978), Private Communication.
- Pyatt, K. D. and J. C. Baker (1978), Private Communication.
- Pyatt, K. D. (1966), "Nuclear Explosion Interaction Studies Vol. II, Methods for Analysis of Thermal Phenomena," General Atomic Final Report GA-7370, AFWL-TR-66-108.
- Rodi, W. L., J. M. Savino, T. G. Barker, S. M. Day, and T. C. Bache (1978), "Analysis of Explosion Generated Surface Waves in Africa, Results from the Discrimination Experiment and Summary of Current Research," Systems, Science and Software Quarterly Technical Report SSS-R-78-3653, April 1978.
- Swanger, H. J. and D. M. Boore (1978), "Simulation of Strong Motion Displacements Using Surface Wave Modal Superposition," Bull. Seism. Soc. Am., 68, in press.
- Wiggins, R. A. (1976), "A Fast, New Computational Algorithm for Free Oscillations and Surface Waves," Geophys. J. R. Astr. Soc., 46, 135-150.